Check for updates

Paleoceanography and Paleoclimatology

RESEARCH ARTICLE
10.1029/2026PA005515

Hydroclimate Variability in the Western Pacific Warm Pool Over the Last 15 kyr

Botond Lázár[1,2,3,4], Mahyar Mohtadi[5], Yu-Chen Yang[1], Jun Hu[1], Enno Schefuß[5], Zhimin Jian[6], Yusuke Yokoyama[7], John R. Southon[8], and Stephan Steinke[1,2]

[1]Department of Geological Oceanography, College of Ocean and Earth Sciences, Xiamen University, Xiamen, China, [2]State Key Laboratory of Marine Environmental Science, College of Ocean and Earth Sciences, Xiamen University, Xiamen, China, [3]Research Center for Integrated Geological Studies, Department of Geology, Babeş-Bolyai University, Cluj-Napoca, Romania, [4]Now at Institute of Geology and Mineralogy, University of Cologne, Cologne, Germany, [5]MARUM-Center for Marine Environmental Sciences, University of Bremen, Bremen, Germany, [6]State Key Laboratory of Marine Geology, Tongji University, Shanghai, China, [7]Atmosphere and Ocean Research Institute and Department of Earth and Planetary Sciences, University of Tokyo, Tokyo, Japan, [8]W. M. Keck Carbon Cycle Accelerator Facility, University of California Irvine, Irvine, CA, USA

Abstract The Western Pacific Warm Pool (WPWP) is the heat engine of the global climate system and has a major impact on the tropical hydroclimate, yet rainfall reconstructions from this core region remain scarce. Here, we present multi-proxy hydroclimate reconstructions from marine sediment core GeoB17429-2, recovered off the coast of northern Papua New Guinea (PNG). We integrate compound-specific plant-wax-derived hydrogen and carbon isotopes with sediment element ratios over the past 15 ka together with isotope-enabled Community Earth System Model 1.2 simulations. All our rainfall proxy records consistently document a distinct Middle Holocene (MH) dry interval (~7–4 ka BP), expressed by enriched plant-wax isotope values indicative of reduced rainfall, and low terrigenous input reflecting less riverine discharge. We suggest that the decrease in rainfall over northern PNG is related to more La Niña-like conditions or alternatively a reduced frequency of El Niño during the MH time interval ~7–4 ka BP. Principal component (PC1) analysis of precipitation-sensitive proxy records across the Maritime Continent (MC) identifies a dominant hydroclimate mode characterized by contrasting rainfall pattern with dry conditions over northern PNG and southwestern regions concurrent with wetter conditions in Borneo and Sulawesi. This mode is strongly correlated with equatorial September insolation, demonstrating that insolation-driven modulation of El Niño Southern Oscillation (ENSO)-like variability could have controlled the Holocene rainfall patterns in the WPWP. Our results demonstrate the sensitivity of PNG rainfall to orbitally forced changes in ENSO-like activity and Walker Circulation strength during the MH.

Plain Language Summary Rainfall changes over the Maritime Continent (MC) influences ecosystems, water resources, and atmospheric circulations throughout the tropical Pacific, yet records from its eastern sector remain limited. Here, we reconstructed rainfall changes over the last ~15,000 years from marine sediment core offshore northern Papua New Guinea. Our record indicates a pronounced decrease in rainfall between ~7,000 and 4,000 years before present. Climate simulations support this interpretation and reveal drier conditions during this interval. Comparison with rainfall records across the MC suggest that this drying occurred alongside wetter conditions in neighboring regions, reflecting a large-scale reorganization of tropical rainfall. We suggest that these hydroclimate changes are connected to a stronger Pacific Walker Circulation and a more persistent La Niña-like conditions during the MH. These results suggest that changes in the tropical Pacific mean state played a central role in shaping rainfall patterns across the MC during the MH and provide valuable context for understanding future hydroclimate changes.

Key Points:

- Pronounced decrease in rainfall in northern Papua New Guinea (PNG) during the Middle Holocene (MH) (~7–4 ka BP)
- Stronger Pacific Walker Circulation (PWC) and La Niña-like conditions reduced rainfall over northern PNG during the MH
- Maritime Continent (MC) records reveal heterogeneous rainfall response to insolation driven changes in El Niño-Southern Oscillation

Supporting Information:

Supporting Information may be found in the online version of this article.

Correspondence to:

S. Steinke,
ssteinke@xmu.edu.cn

Citation:

Lázár, B., Mohtadi, M., Yang, Y.-C., Hu, J., Schefuß, E., Jian, Z., et al. (2026). Hydroclimate variability in the Western Pacific Warm Pool over the last 15 kyr. *Paleoceanography and Paleoclimatology*, *41*, e2026PA005515. https://doi.org/10.1029/2026PA005515

Received 15 APR 2026
Accepted 1 OCT 2026

Author Contributions:

Conceptualization: Mahyar Mohtadi, Zhimin Jian, Stephan Steinke
Data curation: Botond Lázár
Formal analysis: Botond Lázár, Yu-Chen Yang, Jun Hu, Enno Schefuß, Yusuke Yokoyama
Funding acquisition: Mahyar Mohtadi, Enno Schefuß, Zhimin Jian, Stephan Steinke
Investigation: Botond Lázár, Yu-Chen Yang, Jun Hu, Enno Schefuß, Yusuke Yokoyama
Methodology: Botond Lázár, Yu-Chen Yang, Jun Hu, Enno Schefuß, Yusuke Yokoyama, John R. Southon
Project administration: Stephan Steinke
Software: Yu-Chen Yang, Jun Hu
Supervision: Mahyar Mohtadi, Stephan Steinke

© 2026 American Geophysical Union. All rights reserved, including rights for text and data mining and training of artificial intelligence technologies or similar technologies.

1. Introduction

The Western Pacific Warm Pool (WPWP) is the largest reservoir of warm surface waters on Earth with mean annual sea surface temperature (SST) above 28°C (Locarnini et al., 2013) and is considered the steam engine that drives atmospheric circulation on our globe (De Deckker, 2016). It represents a major heat source for the global atmosphere and is a location of deep atmospheric convection and heavy rainfall. Small SST variations in the WPWP influence the location and strength of convection in the rising limb of the Hadley and Walker Circulations, perturbing planetary scale atmospheric circulation, global atmospheric heating, and tropical hydrology (Wang

25724525, 2026, 10, Downloaded from https://agupubs.onlinelibrary.wiley.com/doi/10.1029/2026PA005515 by Xiamen University, Wiley Online Library on [28/10/2026]. See the Terms and Conditions (https://onlinelibrary.wiley.com/terms-and-conditions) on Wiley Online Library for rules of use; OA articles are governed by the applicable Creative Commons License

Validation: Botond Lázár
Writing – original draft: Botond Lázár, John R. Southon, Stephan Steinke
Writing – review & editing: Botond Lázár, Mahyar Mohtadi, Yu-Chen Yang, Jun Hu, Enno Schefuß, Zhimin Jian, Yusuke Yokoyama, John R. Southon, Stephan Steinke

and Mehta, 2008). Thus, the WPWP is a key global vapor source that influences rainfall changes in the middle and low latitudes. The main climate controls on seasonal rainfall changes are the Australian-Indonesian monsoon (AIM) system (e.g., Neale and Slingo, 2003), migration of the Intertropical Convergence Zone (e.g., Schneider et al., 2014), variability of the Southern Pacific Convergence Zone (SPCZ) (e.g., Brown et al., 2020), and changes in the Hadley and Walker Circulation (e.g., Donohoe et al., 2013). On the interannual time-scale, rainfall and ocean conditions are predominantly controlled by changes in the El Niño–Southern Oscillation (e.g., Jia et al., 2016).

Evidence for past rainfall based on proxy records from the MC indicates complex regional-scale variability during the Holocene and the last deglaciation. Rainfall changes as inferred from stable hydrogen and carbon isotopic compositions (δ^2H and δ^{13}C) of terrestrial plant waxes from a marine sediment core from the Nias basin, off Sumatra are interpreted to reflect swings of the mean state of the Indian Ocean Zonal Mode during the Holocene (Niedermeyer et al., 2014a). More to the east toward the center of the MC, river run-off proxy data suggest a drier early to MH compared with the late Holocene (wetter conditions after ∼3 ka) in southern Indonesia (Mohtadi et al., 2011a; Steinke et al., 2014), similar to the δ^{18}O record of speleothems in Flores (Griffiths et al., 2009a). However, speleothem δ^{18}O records from Borneo reveal wetter conditions during the MH (Carolin et al., 2013a; Chen et al., 2016a). This ensemble of records likely indicates a northward shift/displacement of the austral summer rainfall (ITCZ) during the MH (Griffiths et al., 2009a). Oxygen isotopic data in stalagmites from cave KNI-51, located in the eastern Kimberley region of tropical Western Australia suggest enhanced rainfall during the MH (∼7.5–4.5 ka) compared with the late Holocene, which is inconsistent with changes in the position and/or organization of the austral summer rainfall (Denniston et al., 2013). Denniston et al. (2013) suggest that the El Niño/Southern Oscillation (ENSO) may have played a dominant role in driving Australian-Indonesian summer monsoon variability since at least the MH. In contrast, riverine run-off proxy records from the Timor Sea reveal wetter conditions during the early Holocene compared to the middle-late Holocene, which is interpreted to reflect a southward ITCZ shift during the early Holocene and northward shifts of the ITCZ during the MH (Kuhnt et al., 2015). In the same way, Australian lake sediments also indicate wetter conditions than today during the early and MH (Nott and Price, 1994).

While numerous rainfall reconstructions exist from western to central part of the MC (e.g., Dubois et al., 2014; Parish et al., 2024a; Ruan et al., 2019; Russell et al., 2014; Tierney et al., 2012a; Wicaksono et al., 2017), proxy records from the eastern sector (i.e., PNG) remain scarce Moreover, the aforementioned rainfall reconstructions show heterogenous patterns, which hamper our understanding of rainfall variations and their climatic forcing in the WPWP during the Holocene and last deglaciation. Proxy indicators of continental (bulk marine sediment Fe/Ca and Ti/Ca ratios) and marine rainfall and advection (sea surface salinity, SSS) from a sedimentary archive off the northern coast of PNG reveal a minimum in rainfall driven runoff and erosion during the MH (i.e., from 8 to 6 ka BP), followed by an abrupt transition, within ∼1 ka, to wetter conditions during the Late Holocene (Bova et al., 2025). Bova et al. (2025) invoke a contraction of the tropical rain band and a MH strengthening of the PWC to explain rainfall variability in the WPWP during the Holocene.

Here we present plant-wax-based rainfall reconstructions from northern PNG located in the WPWP, which provides an insight into the mechanisms driving Holocene rainfall variability in this region. We analyzed plant-wax-derived *n*-alkanes and their stable carbon (δ^{13}C) and hydrogen (δ^2H) isotopic compositions, alongside runoff-sensitive sediment elemental ratios (Fe/Ca and Ti/Ca) obtained by X-Ray Fluorescence (XRF) core scanning from marine sediment core GeoB17429-2. The core site is located ∼25 km off the northern coast of PNG and ∼60 km west of the Sepik and Ramu River mouths. Situated within the WPWP, center of the intricate ocean-atmosphere coupling, our core location is ideally positioned to capture and study past rainfall variability and its potential underlying drivers in this region. To complement our multi proxy-based reconstruction of Holocene rainfall and sediment discharge in the Sepik-Ramu catchment area (see Figures 1b–1d), we conducted isotope-enabled Community Earth System Model (iCESM) 1.2 simulations to further investigate rainfall dynamics across the WPWP. Our new rainfall record reveals distinct rainfall patterns throughout the Holocene, highlighting the complexity of hydroclimate changes in the WPWP.

1.1. Modern Climate and Vegetation

Rainfall in PNG is predominantly affected by the complex interactions between the position of the ITCZ, the seasonal strengthening of the AIM system, ENSO (e.g., De Deckker, 2016; Smith et al., 2013), and the Southern

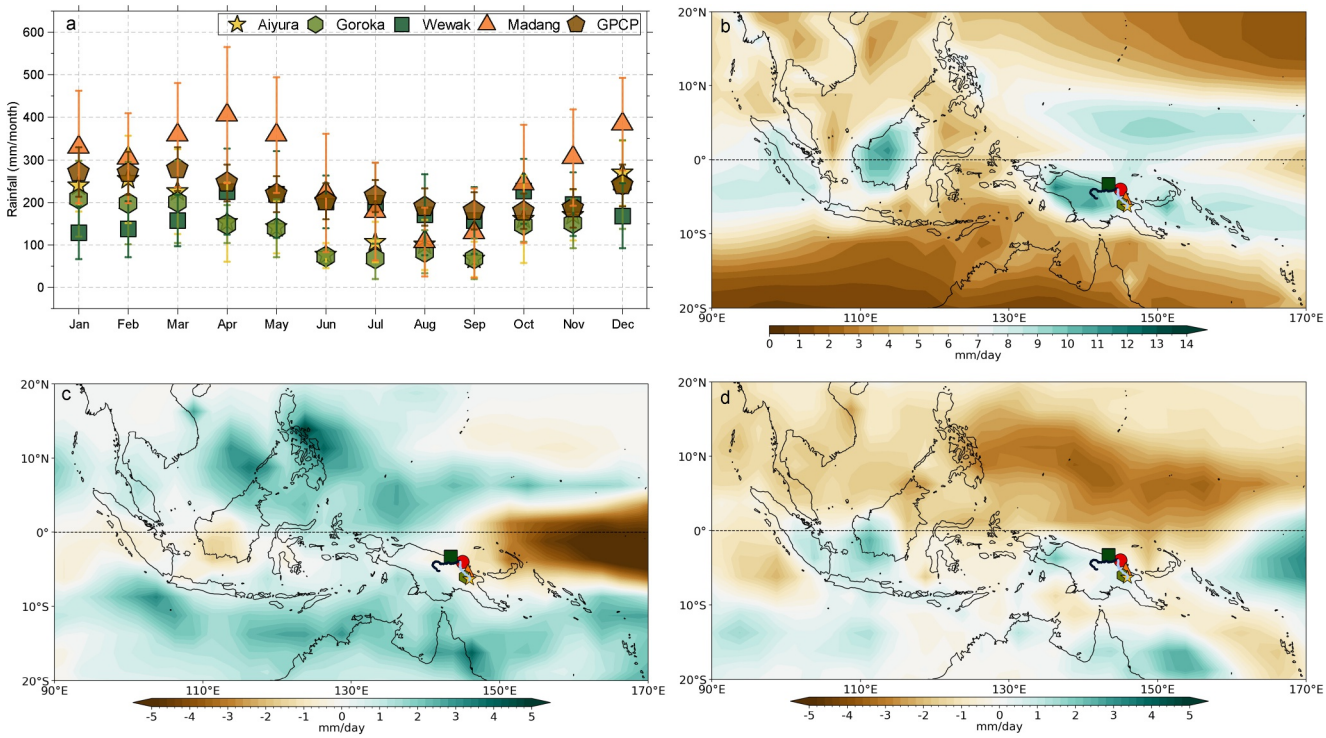


Figure 1. Modern rainfall variability across the Maritime Continent (MC), (a) Monthly rainfall data from meteorological stations Aiyura (yellow star), Goroka (light green hexagon), Wewak (dark green square), Madang (orange triangle), and Global Precipitation Climatology Project (GPCP; 1979–2024, brown pentagon) over Papua New Guinea (PNG) (0–13°S, 140–160°E; Adler et al., 2003). Error bars show standard deviations; (b) Long-term, mean precipitation (mm/day) across the MC based on GPCP (1979–2024); (c) La Niña (years 1998, 1999, 2000, 2010, and 2020) and; (d) El Niño (1982, 1997, 2009, 2015, and 2024) rainfall anomalies (mm/day). The red dot marks the investigated core location, while the symbols and colors are consistent across the panels. The two major rivers systems are indicated with dark blue (Sepik), and light blue (Ramu) colors. Note the higher (lower) rainfall over northern PNG occurs during El Niño (La Niña) years.

Pacific Convergence Zone (SPCZ) strength and position (e.g., Brown et al., 2020). Due to the location of PNG within the WPWP, PNG receives constant rainfall year-around but for most parts of PNG, rainfall maxima occur during November-April (Aldrian & Dwi Susanto, 2003, see below), when the ITCZ shifts southward and the AIM strengthens. During the austral summer season, all parts of the island are almost continuously experiencing high rainfall. Global Precipitation Climatology Project (GPCP; 1979–2024) satellite-based, and in situ rainfall data from different meteorological stations and varying altitudes from PNG reveal seasonal and altitudinal difference in monthly precipitation over PNG. Both the in situ rainfall measurements and the long-term GPCP precipitation data display generally high rainfall amounts during the austral summer-to-autumn (December to May) and drier conditions during the austral winter (June-September; see Figure 1c). Monthly mean precipitation in highland areas, such as Aiyura and Goroka varies between 30 and 400 mm, while lowland areas (Madang and Wewak) receive between ∼15 and 700 mm monthly mean precipitation. Generally, relatively high rainfall occurs between October and May (varying from ∼150 to 400 mm/month), while from June to September relatively low rainfall (∼70–200 mm/month) is registered.

In addition, ENSO events cause significant interannual variations in rainfall over the NG region. Rainfall data from the NG based on meteorological observation, reanalysis products, and satellite-based Tropical Rainfall Measuring Mission data reveal local differences in the WPWP response to ENSO (Rauniyar and Walsh, 2013; Smith et al., 2013). Despite the changes in large-scale subsidence and ascent associated with the Walker Circulation, which dominates the climate over the WPWP during the opposing phases of ENSO, most of the larger islands (e.g., Sumatra, Borneo, and NG) exhibit a dipole structure in rainfall distribution that depends on the local geography and orography (Rauniyar and Walsh, 2013). Certain island of the MC, such as northeastern and southeastern PNG and southwestern Borneo and Sumatra experience more (less) rainfall during El Niño (La Niña) years (Qian et al., 2010, 2013; Rauniyar and Walsh, 2013; Smith et al., 2013). However, the precipitation patterns across NG is spatially heterogeneous. Rauniyar and Walsh (2013) reported no significant differences in

25724525, 2026, 10, Downloaded from https://agupubs.onlinelibrary.wiley.com/doi/10.1029/2026PA005515 by Xiamen University, Wiley Online Library on [28/10/2026]. See the Terms and Conditions (https://onlinelibrary.wiley.com/terms-and-conditions) on Wiley Online Library for rules of use; OA articles are governed by the applicable Creative Commons License

25724525, 2026, 10, Downloaded from https://agupubs.onlinelibrary.wiley.com/doi/10.1029/2026PA005515 by Xiamen University, Wiley Online Library on [28/10/2026]. See the Terms and Conditions (https://onlinelibrary.wiley.com/terms-and-conditions) on Wiley Online Library for rules of use; OA articles are governed by the applicable Creative Commons License

rainfall between El Niño and La Niña years within the central mountain range of NG. In contrast, precipitation on either side of this mountain range exhibits opposing responses to ENSO variability. The southern lowland receives above-average (below-average) rainfall during La Niña (El Niño) years, whereas the northern lowlands, including the Sepik and Ramus River catchments, experiences the opposite pattern. These rainfall anomalies are linked to changes is atmospheric circulation, with enhanced (reduced) low-level convergence over the southern (northern) lowland during La Niña events and a reversal of this pattern during El Niño years (Rauniyar and Walsh, 2013). Consistent with these findings, Smith et al. (2013) showed that eastern Irian Jaya and western PNG tend to be drier during El Niño events, whereas northeastern and southeastern PNG become wetter. In contrast, the New Ireland and New Britain regions exhibit reduced rainfall during both El Niño and La Niña years.

The highest elevation in PNG is located at Mount Wilhelm and reaches ∼4,500 m. The vegetation is strongly altitudinally zoned, with transitions from lowland rainforest to montane forest, Ericaceous shrubland, and alpine grassland chiefly controlled by temperature along the steep elevation gradient of the New Guinea Highlands (Hope, 2014; Paijmans, 1976). The coastal area of PNG is mainly dominated by strand vegetation and mangroves along with some grasses and sedges (Lentfer et al., 2010). Above this, the lowland zone (up to 1,000 m) can be considered a tropical rainforest with diverse tree species and palms (Whitfeld et al., 2014). With increasing elevation, the lower montane forests are transitioning into mid-montane zones, characterized by tree ferns, conifers and mosses (Hope, 2014). The upper montane forest is marked by stunted trees, Rhododendron, and Ericaceae, transitioning into a subalpine forest and alpine grassland above 3,200 m, where grasses, sedges and dwarf shrubs prevail (Bourke, 2010).

2. Materials and Methods

2.1. Site Description and Age Model

Sediment core GeoB17429-2 (4°6.032′S, 145°12.029′E; 1604 m water depth, core length 590 cm) was recovered from the Bismarck Sea, offshore northern PNG during the RV SONNE Cruise SO-228 in 2013 (Mohtadi et al., 2013). Sedimentological description of the core revealed dark olive gray nannofossil-bearing mud with numerous cm-scale ash layers (Mohtadi et al., 2013). Age control for core GeoB17429-2 is based on 16 Accelerator Mass Spectrometry radiocarbon dates (see Table 1, Figure 2). AMS ^{14}C-datings were performed either on monospecific samples of planktic foraminifera *Trilobatus sacculifer* or on mixed *Globigerinoides ruber* and *T. sacculifer* samples. Radiocarbon ages were measured at the W. M. Keck Carbon Cycle Accelerator Facility, University of California Irvine, Irvine, USA and at the Analytical Center for Environmental Science, Atmosphere and Ocean Research Institute, University of Tokyo, Japan. A continuous depth-age model was built with a Bayesian approach using the software *R* version 4.2.3 (Blaauw & Christen, 2011). Each radiocarbon date was converted to calendar years with the rBacon (Blaauw & Christen, 2011) package using the Marine20 calibration curve with a standard marine reservoir correction of 550 years and applying a local reservoir age correction of $\Delta R = -54 \pm 132$ years (Chappell & Polach, 1976; McGregor et al., 2008; Petchey et al., 2013; Petchey and Ulm, 2012; Ulm et al., 2023). Based on our age model, core GeoB17429-2 covers the last ∼15,000 years. Highest sedimentation rates occurred between ∼15 and 10 ka BP (∼48 cm/kyr), with lowest sedimentation rates between ∼10 and 4 ka BP (∼31 cm/kyr), followed by increased sedimentation rates to ∼40 cm/kyr after ∼4 ka BP.

2.2. Alkane Extraction and Analysis

Samples of core GeoB17429-2 (∼10 g of sediment) were freeze-dried, ground, and homogenized into a fine powder. In total 50 samples (plus 5 duplicates were re-sampled and re-measured from randomly used intervals) were prepared and analyzed for plant wax biomarkers. The average sample resolution is around 12 cm (∼0.29 ka). Before extraction an internal standard was added. Plant waxes were extracted using a DIONEX ASE200 (three, five-minute cycles, using Dichloromethane (DCM): Methanol (MeOH)–9:1 at 100°C and 1,000 psi). The total lipid extracts were saponified with the help of 0.1 M KOH-solution and neutral fractions were recovered with hexane. Neutral lipid fractions were separated by column chromatography (Pasteur pipettes with 4 cm deactivated silica) using hexane, DCM, and DCM: MeOH–1:1 as solvents, obtaining the hydrocarbon, ketone, and polar fractions. Purification and removal of the unsaturated compounds from the hydrocarbon fractions were achieved by column chromatography over $AgNO_3$-coated silica, using hexane as eluent to obtain saturated hydrocarbon fractions. Prior to isotope analysis, saturated hydrocarbon fractions were analyzed using a Thermo Scientific

25724525, 2026, 10, Downloaded from https://agupubs.onlinelibrary.wiley.com/doi/10.1029/2026PA005515 by Xiamen University, Wiley Online Library on [28/10/2026]. See the Terms and Conditions (https://onlinelibrary.wiley.com/terms-and-conditions) on Wiley Online Library for rules of use; OA articles are governed by the applicable Creative Commons License

Table 1
AMS-^{14}C Ages and Calendar Ages of Core GeoB17429-2

Lab label	Depth (cm)	Foraminifera species	^{14}C age (yr BP)	± yr	Cal. Age (yr BP)	±1-σ (68%)[a]	±2-σ (95%)[a]
UCIAMS-142704[b]	2	*T. sacculifer*	550	20	147	0–189	0–347
UCIAMS -150611[b]	6	*G. ruber* + *T. sacculifer*	725	15	232	95–378	0–462
UCIAMS -142705[b]	58	*T. sacculifer*	1,945	20	1,405	1,254–1,559	1,093–1,724
UCIAMS -150612[b]	74	*G. ruber* + *T. sacculifer*	2,225	15	1,756	1,537–1,881	1,376–2,060
UCIAMS -150615[b]	98	*G. ruber* + *T. sacculifer*	2,760	15	2,334	2,194–2,576	2,027–2,726
UCIAMS -150616[b]	122	*G. ruber* + *T. sacculifer*	3,140	15	2,866	2,687–3,030	2,480–3,208
YAUT-095803[c]	166	*G. ruber* + *T. sacculifer*	3,962	28	3,912	3,666–4,054	3,471–4,234
YAUT-095804[c]	210	*G. ruber* + *T. sacculifer*	4,823	30	5,059	4,808–5,184	4,582–5,323
UCIAMS -150617[b]	258	*G. ruber* + *T. sacculifer*	6,240	15	6,542	6,379–6,704	6,235–6,878
YAUT-095805[c]	286	*G. ruber* + *T. sacculifer*	7,205	30	8,514	7,411–7,688	7,268–7,839
YAUT-095806[c]	334	*G. ruber* + *T. sacculifer*	8,536	36	8,991	8,848–9,253	8,630–9,399
YAUT-095809[c]	366	*G. ruber* + *T. sacculifer*	9,169	39	9,903	9,592–10,006	9,466–10,184
UCIAMS -150618[b]	374	*G. ruber* + *T. sacculifer*	10,080	45	10,169	10,818–11,235	10,598–11,469
UCIAMS -150619[b]	458	*G. ruber* + *T. sacculifer*	10,680	25	11,924	11,701–12,183	11,485–12,425
YAUT-095811[c]	510	*G. ruber* + *T. sacculifer*	11,564	40	12,995	12,791–13,080	12,673–13,235
UCIAMS -150620[b]	574	*G. ruber* + *T. sacculifer*	12,965	40	14,483	14,487–15,003	14,205–15,187

[a]Calibrated with CALIB 8.2 and the Marine20 data set (Heaton et al., 2020). [b]Measured at the W. M Keck Carbon Cycle Accelerator Facility, Earth System Science Department, University of California Irvine, Irvine, United States of America. [c]Measured at the Analytical Center for Environmental Science, Atmosphere and Ocean Research Institute, University of Tokyo, Japan.

Focus gas chromatograph equipped with a flame ionization detector (GC-FID) to identify and quantify individual *n*-alkanes. Compounds were identified by comparison of retention times with an external alkane standard mixture (*n*-C_{16}–*n*-C_{34}) and concentrations were used to optimize sample dilutions and ensure appropriate signal intensities for subsequent GC-IRMS analysis. Plant-wax distributions were dominated by the long-chain *n*-C_{31} alkane, with the *n*-C_{29} and *n*-C_{33} alkane occurring in secondary abundance (Figure S1 in Supporting Information S1) with the distinct odd-over-even chain-length distribution of plant-waxes (Eglinton and Hamilton, 1967). Carbon preference index (CPI, C_{25}–C_{33}) values remained elevated throughout the record, ranging from 2.9 to 6 (Figure S2 in Supporting Information S1). $\delta^{13}C$ measurements were performed on a Thermo Trace GC Ultra equipped with a HP-5 ms column coupled to a FinniganMAT 252 isotope ratio monitoring mass spectrometer (MS) via a combustion interface operated at 1,000°C using helium carrier gas at MARUM, University Bremen. The $\delta^{13}C$ values were calibrated against an external reference CO_2 gas calibrated against carbonate standards including NBS-19 on a dual-inlet MAT 253 plus using a Kiel IV carbonate device. $\delta^{13}C$ values of the *n*-alkanes are reported in permille (‰) against Vienna PeeDee Belemnite (VPDB). $\delta^{2}H$ analyses were conducted using a Thermo Trace GC equipped with a HP-5 ms column connected to a MAT 253 isotope MS via high-temperature pyrolysis reactor operated at 1420°C using helium carrier gas at MARUM. H_2 reference gas calibrated on a TCEA-IRMS using IAEA water standards including VSMOW. The $\delta^{2}H$ *n*-alkanes values are reported as permil (‰) relative to VSMOW (Vienna Standard Mean Ocean Water). The H_3^+ -factor was measured daily and was 5.58 ± 0.04 throughout the measurement period. Instrumental performance of both systems was monitored using an in-house *n*-alkane mixture (*n*-C_{16}–*n*-C_{34}) measured every sixth sample. The isotopic composition of the in-house standard mixture was calibrated against known *n*-alkane standards (e.g., A2, A3, and B2 from A. Schimmelmann, Indiana University). Measurements were conducted only when the absolute deviation of all individual standard

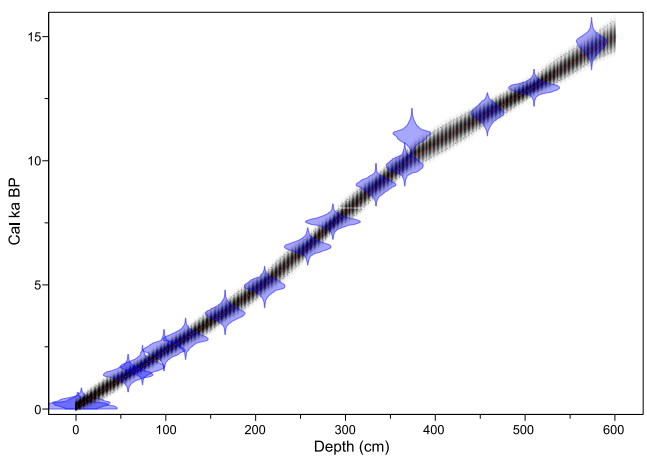


Figure 2. Age-depth relationship of gravity core GeoB17429-2. The age depth relationship was built with a Bayesian approach using rBacon (Blaauw & Christen, 2011) overlying the distributions of the individual dates (blue). Line curve shows the best model (red dotted line: mean), gray-scales indicate chronological uncertainties (gray dotted lines: the model's 95% probability interval).

25724525, 2026, 10, Downloaded from https://agupubs.onlinelibrary.wiley.com/doi/10.1029/2026PA005515 by Xiamen University, Wiley Online Library on [28/10/2026]. See the Terms and Conditions (https://onlinelibrary.wiley.com/terms-and-conditions) on Wiley Online Library for rules of use; OA articles are governed by the applicable Creative Commons License

compounds from accepted values remained below 3.0‰ for δ^2H and 0.3‰ for $\delta^{13}C$. This acceptance criteria described by Kahmen et al. (2013a, 2013b) results in a scale normalization factor of 1 when using calibrated reference gases and calibrated in-house alkane standard as performance check and avoid artifacts when using degraded reactors (Wang and Sessions, 2008). Due to low compound abundances, 40 samples were measured in duplicates and 10 samples only once for δ^2H. Similarly, 36 samples were measured in duplicates and 14 samples were measured once for $\delta^{13}C$. For single measurements, long-term reproducibility of external standards (i.e., ±3‰ for δ^2H and ±0.3‰ for $\delta^{13}C$) was assumed as analytical uncertainty. Replicate measurements demonstrate high analytical reproducibility, with average uncertainties of ∼1‰ for δ^2H and ∼01.–0.2‰ for $\delta^{13}C$ for individual homologs. Maximum deviations are 4‰ for δ^2H and 0.6‰ for $\delta^{13}C$. δ^2H_{wax} and $\delta^{13}C_{wax}$ were calculated based on the weighted-mean concentrations of the *n*-C_{29}, *n*-C_{31}, and *n*-C_{33} alkanes and their respective δ^2H and $\delta^{13}C$ values. The reported larger propagated uncertainty (e.g., 5‰ for δ^2H) reflects error propagation in weighted averages.

2.3. Isotope Composition (δ^2H_{precip}) Estimation

Vegetation type changes (e.g., C_3 and C_4) can lead to an offset in the δ^2H_{wax} values due to different hydrogen isotopic fractionation (Feakins and Sessions, 2010; Gao et al., 2014; Sachse et al., 2012). For that reason, for each individual *n*-alkane homologue (*n*-C_{29}, *n*-C_{31}, and *n*-C_{33}) apparent fractionation factors were estimated following Collins et al. (2013), using end-member fractionation factors of −125‰ for C_3-type vegetation, and −145‰ for C_4-type vegetation. Relative contributions of C_3 and C_4 vegetations were approximated from the measured $\delta^{13}C_{wax}$ values. Given the limited variability of the $\delta^{13}C_{wax}$ throughout the record (average −33.4‰ ± 0.6‰), resulting apparent hydrogen isotope fractionation factors varied only slightly along the ∼15 ka record. The calculated fractionation factors were subsequently applied to individual samples prior to calculating δ^2H_{precip}. Precipitation isotopes in the western tropical Pacific are influenced by multiple factors and processes, including precipitation amount, convective activity, and moisture transport (Falster et al., 2021; Konecky et al., 2019). To evaluate the reliability of the reconstructed precipitation isotope signal, near-coretop δ^2H_{precip} estimate was compared with both modern precipitation isotope observations and the iCESM pre-industrial (PI) simulation at the core location. Modern precipitation-weighted mean δ^2H values were obtained from the Global Network of Isotopes in Precipitation (GNIP) station at Madang, PNG (Rozanski et al., 1993). Hence, providing independent assessment of the consistency between reconstructed, observed, and simulated precipitation isotopes. The δ^2H_{precip} estimates were corrected for global ice-volume changes using the marine oxygen isotope compilation of Bintanja et al. (2005).

2.4. Bulk Sediment Element Analysis

The bulk sedimentary element composition of core GeoB17429-2 was determined by XRF. XRF Core Scanner data were collected every 2 cm down-core using a generator setting of 20 kV, 0.087 mA and a sampling time of 20 s directly at the split core surface of the archive half with XRF Core Scanner I at MARUM, University of Bremen. The split core surface was covered with a polypropylene foil to avoid contamination of the XRF measurement unit and desiccation of the sediment. Here, the reported data have been acquired by XRF Core Scanner I at MARUM using a KEVEX Psi Peltier Cooled Silicon Detector and a KEVEX X-ray Tube 52500008-02 with the target material molybdenum (Mo).

2.5. Statistical Analysis

We applied Principal Component Analysis (PCA) to a compilation of precipitation-sensitive proxy records (δ^2H, $\delta^{18}O$ and XRF) to identify the dominant modes of hydroclimate variability across the MC (see Table 2). The analysis was restricted to proxies that reflect changes in rainfall amounts. Prior to PCA, all records ($n = 15$) were interpolated to a common temporal resolution of 0.3 ka, standardized using z-scores to remove unit dependence. All analyses were performed using OriginPro 2026 software. The analysis covers the interval from ∼13 ka BP to ∼1 ka BP to maximize temporal overlap among sites. For the data sets of Ruan et al. (2018) and Parish et al. (2024b), δ^2H_{wax} values were calculated using weighted-averages of *n*-C_{29}, *n*-C_{31}, and *n*-C_{33} homologs to avoid site-specific overrepresentation. Only rainfall proxy records with a sufficient temporal span were included in the PCA (i.e., their temporal resolution reached at least 13 ka BP). To evaluate whether the MH (∼7–4 ka BP) enrichment observed in the $\delta^2H_{precip\text{-}ic}$ record is statistically different from the remainder of the record a Monte Carlo framework was performed using *R* (v4.4.2) software that accounted for both analytical (±5‰), and

25724525, 2026, 10, Downloaded from https://agupubs.onlinelibrary.wiley.com/doi/10.1029/2026PA005515 by Xiamen University, Wiley Online Library on [28/10/2026]. See the Terms and Conditions (https://onlinelibrary.wiley.com/terms-and-conditions) on Wiley Online Library for rules of use; OA articles are governed by the applicable Creative Commons License

Table 2
Precipitation-Sensitive Proxy Records Used for Principal Component Analysis (PCA)

Archive	Latitude	Longitude	Proxy type	References
Gunung Buda	4°	115°	Stalagmite	Carolin et al. (2013a), Carolin et al. (2013b)
Bukit Assam Cave	4°	114°5	Stalagmite	Chen et al. (2016a), Chen et al. (2016b)
MD10-3,340	−0°52	128°72	XRF	Dang et al. (2020a), Dang et al. (2020b)
Liang Luar	−8°32	120°26	Stalagmite	Griffiths et al. (2009a), Griffiths et al. (2009b)
GIK18517-2	−1°53663	117°5626	XRF	Hendrizan et al. (2017)
GeoB17419-1	−2°81467	144°49,967	XRF	Hollstein et al. (2019)
TOW10-9B	−2°75	121°5	Plant wax	Konecky et al. (2016)
GeoB10053-7	−8°6765	112°8725	XRF	Mohtadi et al. (2011a), Mohtadi et al. (2011b)
SO189-144 KL	1°093	98°0396	Plant wax	Niedermeyer et al. (2014a), Niedermeyer et al. (2014b)
TOW10-9B	−2°75	121°5	Plant wax	Parish et al. (2024a), Parish et al. (2024b)
GeoB 10,053-7	−8°4059	112°5235	Plant wax	Ruan et al. (2018)
BJ8-03-70GGC	−3°5	119°	Plant wax	Tierney et al. (2012a), Tierney et al. (2012b)
SO18515	−3°6	119°7	Plant wax	Wicaksono et al. (2017)
MD01-2378	−13°0873	121°8042	XRF	Zhang et al. (2020)
GeoB17429-2	−4°6032	145°12029	Plant wax	This study; Lázár et al. (2026)

chronological uncertainties derived from the rBacon age-model (Carré et al., 2012; McClelland et al., 2021; McKay et al., 2021). For each of 10,000 realizations, sample ages were randomly perturbed within their age uncertainties, while $\delta^2H_{precip\text{-}ic}$ values were varied within their analytical uncertainties. For each realization, reconstructed $\delta^2H_{precip\text{-}ic}$ values from the MH (~7–4 ka BP) were compared with those from the remainder of the record using a two-sample Kolmogorov-Smirnov (KS) test. The resulting distribution of the KS statistics and *p*-values were used to assess the robustness of the MH isotope enrichment relative to the propagated analytical and chronological uncertainties.

2.6. Climate Model Simulation

We use the stable water isotope-enabled climate model iCESM1.2 to perform a suite of orbital sensitivity experiments to investigate Holocene hydroclimate and the corresponding rainfall isotope variability. iCESM1.2, is a fully coupled model, comprising an atmospheric component (iCAM5) and a land component (iCLM4) both at a resolution of 1.9° × 2.5° (latitude × longitude), and an ocean component (iPOP2) at 1° × 1°. Water isotopes and their fractionation processes: surface evaporation, vapor condensation/deposition, and rainfall re-evaporation, are explicitly represented in the atmospheric, land, ocean, and sea ice components. We conducted ten time-slice experiments at 1,000-year intervals from 1 ka to 10 ka. The 1 ka experiment is branched from a stable preindustrial control run and integrated for 150 years to ensure it reaches equilibrium. The final state of the 1 ka run is then used to initialize the 2-ka run, and this procedure is repeated through to 10 ka BP. Each of these 10 runs is integrated for 150 years, ensuring that each reaches equilibrium. To minimize the influence of the model adjustment the final 20 years of each 150-year simulation were used. The suit of orbital configuration is set according to the corresponding time slice, while other boundary conditions, such as greenhouse gas concentrations and vegetation, are prescribed at preindustrial levels. To correct the modeled monthly mean precipitation and to account for the calendar effect, which arises because Earth moves faster at perihelion and slower at aphelion, we adjusted the length of each month (Shi et al., 2022). Hence, the daily output was adjusted by the length of each month for all the simulations, and then calculated the monthly mean precipitation based on the adjusted calendar (Bartlein & Shafer, 2019; Shi et al., 2022). To assess model performance, mean annual precipitation from the PI simulation was compared with modern, long term precipitation observations from GPCP (Figure S3 in Supporting Information S1).

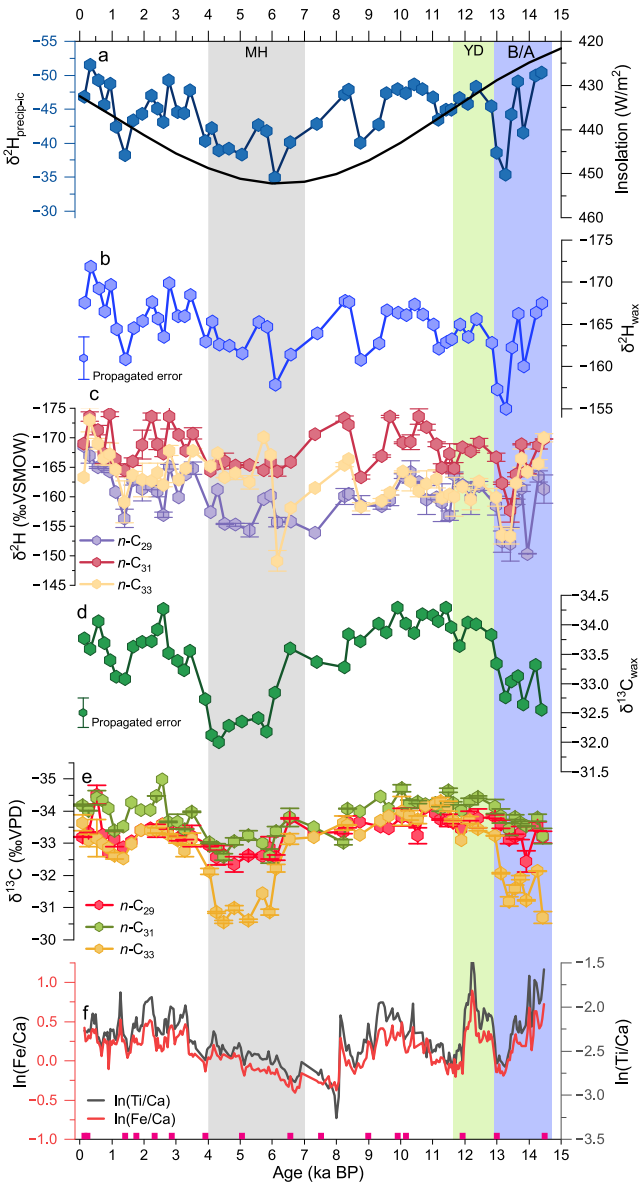


Figure 3. Plant-wax analysis and bulk sediment element data from offshore northern Papua New Guinea. (a) Ice-volume adjusted rainfall estimate ($\delta^2H_{precip\text{-}ic}$) and superimposed is the equatorial September insolation (Laskar et al., 2004); (b) δ^2H_{wax} weighted mean average; (c) δ^2H (n-C_{29}, n-C_{31}, n-C_{33}) data; (d) $\delta^{13}C_{wax}$-weighted mean average; (e) $\delta^{13}C$ (n-C_{29}, n-C_{31}, n-C_{33}) measurements, and (f) X-Ray Fluorescence sediment element ratio: ln (Fe/Ca) (red) and ln (Ti/Ca) (black). Magenta squares indicate the position of the 16 AMS-^{14}C radiocarbon dates for age control. MH: Middle Holocene (gray band); YD: Younger Dryas (green band); B/A: Bølling–Allerød (blue band). Error bars in panel (c and e) represent standard deviations.

3. Results

3.1. Plant-Wax Carbon Isotopes ($\delta^{13}C$) and Hydrogen Isotopes (δ^2H)

The $\delta^{13}C$ measurements of n-C_{29} revealed values between −34.5‰ and −32.3‰ (±0.5), n-C_{31} between −35‰ and −32.6‰ (±0.5), and n-C_{33} between −34.3‰ and −30.6‰ (±1) (Figure 3e). The $\delta^{13}C$ values of n-C_{29} $\delta^{13}C$ display a strong positive correlation with n-C_{31} $\delta^{13}C$ ($r = 0.70$, $p < 0.01$) and n-C_{33} $\delta^{13}C$ ($r = 0.74$, $p < 0.01$). Similarly, n-C_{31} $\delta^{13}C$ is significantly correlated with n-C_{33} $\delta^{13}C$ ($r = 0.78$, $p < 0.001$). $\delta^{13}C_{wax}$ values (Figure 3d) are between −32‰ and −34.3‰ (with an average of −33.5 ± 0.6‰). $\delta^{13}C_{wax}$ shows a good correlation with $\delta^2H_{precip\text{-}ic}$ ($r = 0.50$, $p < 0.001$). δ^2H values of the three investigated n-alkanes (Figure 3c) ranged between −175‰ and −150‰ (±4‰) for n-C_{29}, between −175‰ and −158‰ (±3‰) for n-C_{31}, and for n-C_{33} values are between −173‰ and −149‰ (±4‰). All three investigated homologs are displaying similar trends and changes. The δ^2H values of n-C_{29} positively correlate with those of n-C_{31} ($r = 0.59$, $p < 0.001$) and those of n-C_{33} ($r = 0.57$, $p < 0.001$), while, n-C_{31} δ^2H and n-C_{33} δ^2H are also correlated ($r = 0.50$, $p < 0.001$). δ^2H_{wax} resulted in values from −155‰ (13.26 ka BP) to −172‰ (0.31 ka BP), the average being −165 ± 3‰ (Figure 3b). δ^2H_{precip} varies between −31‰ and −51‰ (average ∼ −43 ± 4‰). The near core top δ^2H_{precip} value (−47‰) is consistent with both the precipitation-weighted GNIP estimate (−49‰) and the iCESM-simulated value (−50‰). The ice-volume corrected precipitation estimates ($\delta^2H_{precip\text{-}ic}$) reveal more enriched values during the late Holocene (−38‰ at ∼1.5 ka BP), MH (−40 ± 3‰, between 7–4 ka BP), at ∼9 ka BP (−41‰) and two short intervals with values of ∼−36‰ (∼13.5 ka BP), and −42‰ (∼14 ka BP, see Figure 3a). Between the last deglaciation (∼14.5 ka BP) and early Holocene $\delta^2H_{precip\text{-}ic}$ deviates from δ^2H_{precip} by −5‰, after which no significant deviation is shown between the two records (see Figure S4 in Supporting Information S1).

3.2. Bulk Sediment Element Analysis

XRF bulk sediment element ratios ln (Ti/Ca) and ln (Fe/Ca) are displaying similar trends, having a strong correlation ($r = 0.97$, $p < 0.001$) along the investigated ∼15 ka. The ln (Ti/Ca) values are between −3.26 and −1.41 (average value −2.34 ± 0.28), while the ln (Fe/Ca) is between −0.41 and 0.90 (average value 0.14 ± 0.24). More negative values occurred during the MH (∼8–4 ka BP; Figure 3f), suggesting less riverine terrigenous supply and thus less rainfall. Individual elemental records are shown in Figure S5 in Supporting Information S1.

3.3. PCA Analysis and $\delta^2H_{precip\text{-}ic}$ Variability

PCA results show that the eigenvalues of the PC1 exceed the Kaiser-Guttman criterion and lies above the broke-stick threshold (Jackson, 1993). PC1 explains approximately 45% of the total variance across the precipitation-sensitive proxy data sets. PC2 explains only ∼13% of the data variance and lies beneath the broken-stick curve. PC1 scores range from −2.90 at 4.5 ka BP to 5.77 at around 12.3 ka BP. Given its dominant contribution to overall variance, PC1 will be the primary focus of the following discussion. A Monte Carlo Kolmogorov-Smirnow analysis was performed on our $\delta^2H_{precip\text{-}ic}$ data using 10,000 realizations. The MH interval (7–4 ka BP) remained significantly different from the rest of the record in 62.49% of realizations ($p < 0.05$), with mean and median p-values of 0.096 and 0.021, respectively.

25724525, 2026, 10, Downloaded from https://agupubs.onlinelibrary.wiley.com/doi/10.1029/2026PA005515 by Xiamen University, Wiley Online Library on [28/10/2026]. See the Terms and Conditions (https://onlinelibrary.wiley.com/terms-and-conditions) on Wiley Online Library for rules of use; OA articles are governed by the applicable Creative Commons License

25724525, 2026, 10, Downloaded from https://agupubs.onlinelibrary.wiley.com/doi/10.1029/2026PA005515 by Xiamen University, Wiley Online Library on [28/10/2026]. See the Terms and Conditions (https://onlinelibrary.wiley.com/terms-and-conditions) on Wiley Online Library for rules of use; OA articles are governed by the applicable Creative Commons License

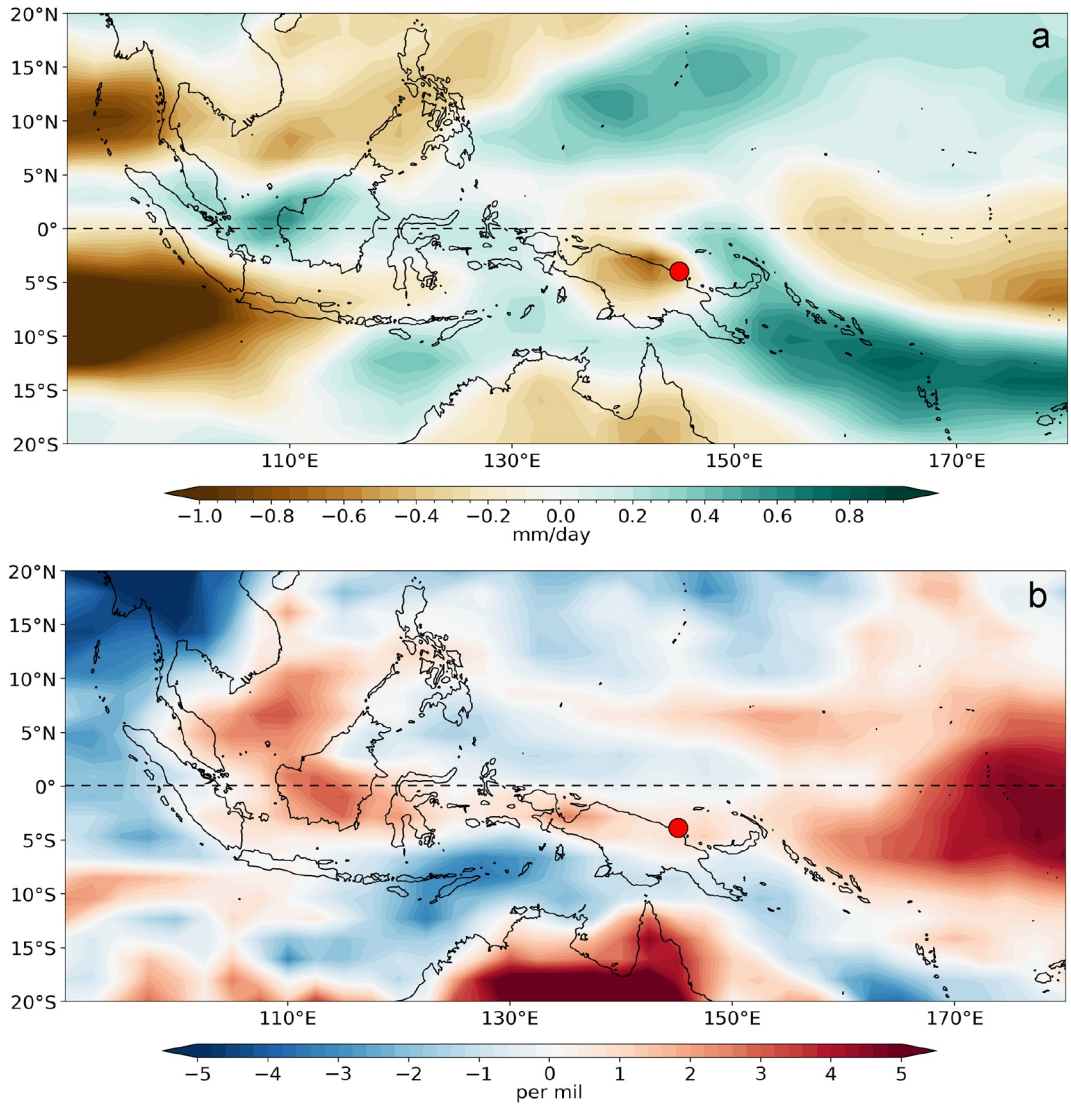


Figure 4. Middle Holocene (7–4 ka BP) annual rainfall and δ^2H anomalies over New Guinea (NG) derived from isotope-enabled Community Earth System Model 1.2 simulations. (a) Averaged 7–4 ka BP minus Pre Industrial rainfall anomaly; and (b) 7–4 ka BP-PI δ^2H anomaly. The model simulations reveal less rainfall and enriched $\delta^2H_{precipitaton}$ over northern NG during the 7–4 ka BP-PI run. The core location is marked with the red dot.

3.4. Climate Model Simulation

We averaged the iCESM1.2 simulated $\delta^2H_{precipitation}$ and rainfall anomalies for 1,000-year intervals spanning 7–4 ka BP (Figure 4), period marked by the largest shift in plant-wax hydrogen isotopes (δ^2H) and carbon isotopes ($\delta^{13}C$), and XRF bulk sediment element ratios, indicating reduced rainfall over NG during this period (see above; Figure 4). The simulation shows enriched $\delta^2H_{precipitation}$ values and decreased rainfall over northern NG during the MH (7–4 ka BP: Figures 4a and 4b). In addition, we conducted a January to December iCESM precipitation simulation for the MH (7–4 ka BP; Figure 5) in order to understand how the annual $\delta^2H_{precipitation}$ (Figure S9 in Supporting Information S1) and rainfall anomalies translate into seasonal changes. We find that the monthly $\delta^2H_{precipitation}$ anomalies (7–4 ka BP minus Pre-Industrial) show enriched values from October to February and depleted values in March to June (Figure S9 in Supporting Information S1). The monthly iCESM rainfall simulation for the MH (7–4 ka BP) show that PNG received less rainfall from November through August, followed by an increase in rainfall from September to October (Figure 5). Moreover, the iCESM-simulated average δ^2H values for the Sepik-Ramu River catchment area closely track the $\delta^2H_{precip\text{-}ic}$ record from GeoB17429-2 (Figure S4 in Supporting Information S1), indicating that the reconstructed $\delta^2H_{precip\text{-}ic}$ primarily tracks long-

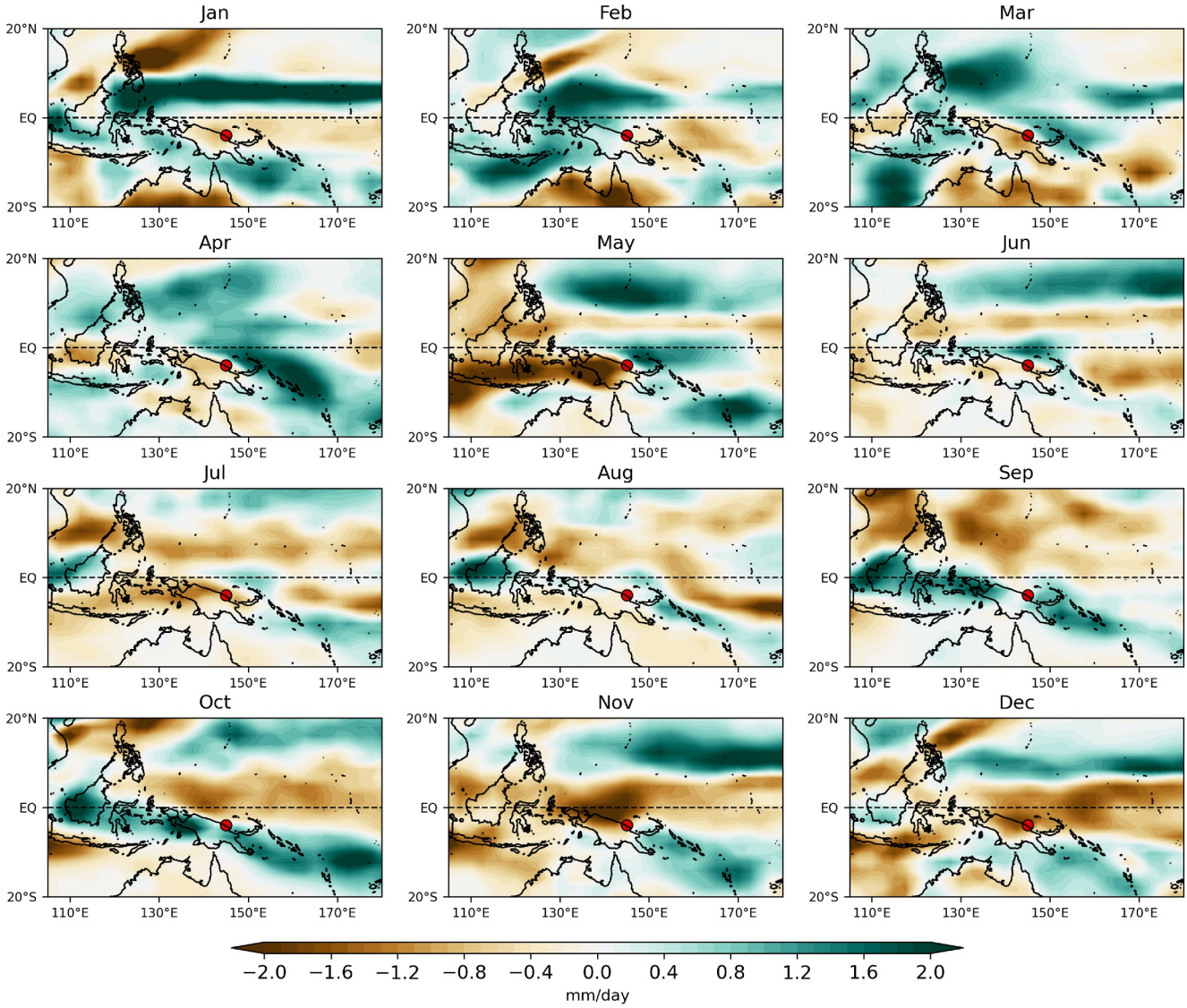


Figure 5. Monthly precipitation anomaly (7–4 ka BP minus pre-industrial) from isotope-enabled Community Earth System Model 1.2 simulations. The simulations reveal reduced rainfall over northern New Guinea during austral summer to autumn, that is November through August. GeoB17429-2 core location is marked with the red dot.

term variability in regional precipitation isotopes. The simulated precipitation isotopes also agree with the modern GNIP observations and near-core top $\delta^2H_{precip\text{-}ic}$ values (see Table S1 in Supporting Information S1), providing independent support to the iCESM simulation.

4. Discussion

4.1. Middle Holocene Decrease in Rainfall Over Northern Papua New Guinea

The most pronounced shift in our biomarker-based δ^2H and $\delta^{13}C$ data set occurs during the MH (~7–4 ka BP). This interval is characterized by relatively enriched $\delta^2H_{precip\text{-}ic}$ values, most likely indicating reduced rainfall, accompanied by less negative (enriched) $\delta^{13}C_{wax}$ values, suggesting changes in vegetation water-use efficiency and likely an increased contribution from C_4 grasses.

$\delta^{13}C$ values are known to be sensitive to physiological responses to water availability, such as stomal conductance and water-use efficiency (Farquhar et al., 1989). Hence, under water-stress (e.g., drier than usual), C_3 plants can register less negative $\delta^{13}C$ values due to reduced stomatal conductance and increased internal CO_2 limitation,

25724525, 2026, 10, Downloaded from https://agupubs.onlinelibrary.wiley.com/doi/10.1029/2026PA005515 by Xiamen University, Wiley Online Library on [28/10/2026]. See the Terms and Conditions (https://onlinelibrary.wiley.com/terms-and-conditions) on Wiley Online Library for rules of use; OA articles are governed by the applicable Creative Commons License

25724525, 2026, 10, Downloaded from https://agupubs.onlinelibrary.wiley.com/doi/10.1029/2026PA005515 by Xiamen University, Wiley Online Library on [28/10/2026]. See the Terms and Conditions (https://onlinelibrary.wiley.com/terms-and-conditions) on Wiley Online Library for rules of use; OA articles are governed by the applicable Creative Commons License

which results in isotopic discrimination (Garcin et al., 2014; Srivastava and Wiesenberg, 2018). Previous studies have proposed *n*-C_{29} as a biomarker for trees and shrubs and *n*-C_{33} as a proxy for grasses (Diefendorf and Freimuth, 2017; Garcin et al., 2014). Hence, the measured enrichment in *n*-C_{33} during the late Holocene (at ∼1.5 ka BP), MH (∼6–4 ka BP), and between ∼15 ka BP and 13 ka BP might reflect a shift in vegetation toward enhanced water-use efficiency and possibly a modest increase in C_4 grasses. In addition, our *n*-alkane data show a chain elongation expressed by higher Norm33 values (see Schefuß et al., 2003), particularly during the MH (∼6–4 ka BP). An increase in the relative contribution of *n*-C_{33} relative to *n*-C_{29} has been associated with greater input from C_4 grasses and more open vegetation in tropical environments (Bush & McInerney, 2013; Garcin et al., 2014; Rommerskirchen et al., 2006). Similar patterns of stronger $\delta^{13}C$ enrichment in *n*-alkanes have been interpreted as an expansion of C_4 grasses off Namibia (Hoetzel et al., 2013). Hence, we suggest that the observed $\delta^{13}C_{wax}$ enrichment (∼6–4 ka BP) primarily reflects increased water stress and enhanced water-use efficiency within C_3 vegetation, potentially accompanied by a modest increase in C_4 vegetation contribution. These trends are consistent with more negative ln (Ti/Ca) and ln (Fe/Ca) ratios during the MH, reflecting less riverine discharge, hence generally less rainfall. Together these proxy records indicate relatively dry conditions over northern PNG during the MH (∼7/6–4 ka BP), although the magnitude and timing of peak values slightly vary among our proxy records. This interpretation is further supported by Monte Carlo KS simulations, since the MH interval remained statistically distinct from the reminder of the record in 62.49% of realizations, with a mean and median p-value of 0.096 and 0.021, respectively (see Figure S6 in Supporting Information S1). Hence, the MH $\delta^{2}H_{precip\text{-}ic}$ values remain statistically distinct from the reminder of the record, demonstrating that the observed isotopic enrichment is unlikely to arise solely from analytical or age uncertainty and supports the interpretation of a MH (∼7–4 ka BP), relatively dry interval.

Modern observations show that rainfall over PNG is controlled by the complex interactions between the seasonal variability of the AIM system, migration of the ITCZ, changes in the SPCZ, and ENSO events (e.g., Brown et al., 2020; Lintner and Boos, 2019; Smith et al., 2013; Tuckman et al., 2024). These interactions are leading to the formation of distinct spatial and seasonal rainfall patterns across the MC (Aldrian & Dwi Susanto, 2003). Based on this, the MC can be divided into three distinct rainfall zones (Figure S7 in Supporting Information S1), each responding differently to boreal (austral) winter (summer) monsoon intensification and to seasonal migration of the ITCZ (see Aldrian & Dwi Susanto, 2003). Within this framework, PNG and northern part of Australia experience a strong monsoonal influence during the austral summer, when the southward-shifted ITCZ enhances moisture transport and produces heavy rainfall. An ITCZ-driven hydroclimate change is evidenced in the northern Borneo speleothem records (e.g., Carolin et al., 2013a; Chen et al., 2016a), which document a wetter MH, consistent with a northward-shifted ITCZ. Such displacement could theoretically explain wetter conditions in northern Borneo, and reduced rainfall in PNG and across northern Australia. However, stalagmite records from northern Australia show contrasting MH responses, with some records indicating wetter conditions (Denniston et al., 2013), and others suggesting drier conditions associated with a weakened Australian summer monsoon (Shi et al., 2025). These contrasting responses indicate that MH rainfall patterns cannot be explained solely by ITCZ migration. Additionally, a contraction of the tropical rain belt driven by changes in PWC strength has been proposed recently by Bova et al. (2025). However, narrower rainfall band would lead to drier conditions across northern Australia, consistent with Shi et al. (2025), but incompatible with the enhanced MH rainfall recorded by Denniston et al. (2013). Consequently, given these inconsistencies in spatial rainfall patterns, we conclude that ITCZ migration alone cannot account for the MH hydroclimate variability, and therefore we will explore alternative forcing scenarios.

Besides the interaction of ITCZ and AIM, ENSO exerts strong control on rainfall patterns over PNG (see above). As noted above, in modern climatology, certain regions of PNG, such as northeastern and southeastern PNG experience more (less) rainfall during El Niño (La Niña) years. It might be therefore possible, that either a reduced El Niño frequency and/or more prevalent La Niña-like conditions caused the reduction in rainfall over northern PNG during the MH time interval ∼7–4 ka BP. To assess whether a reduced El Niño frequency and/or more prevalent La Niña-like conditions might have exerted a dominant control on the MH reduction in rainfall over northern PNG, we compare our records with the Holocene zonal (west-east) SST gradient anomaly based on the difference of western and eastern equatorial Pacific *G. ruber* Mg/Ca- SST records taken from Koutavas and Joanides (2012a, 2012b). The MH (∼7–4 ka BP) interval of enriched $\delta^{2}H_{precip\text{-}ic}$ values coincides with enhanced zonal equatorial SST gradient (see Figure 6b), suggesting La Niña-like conditions (e.g., Koutavas and Joanides, 2012a; Marchitto et al., 2010), which might have resulted in less rainfall in northern PNG during the MH.

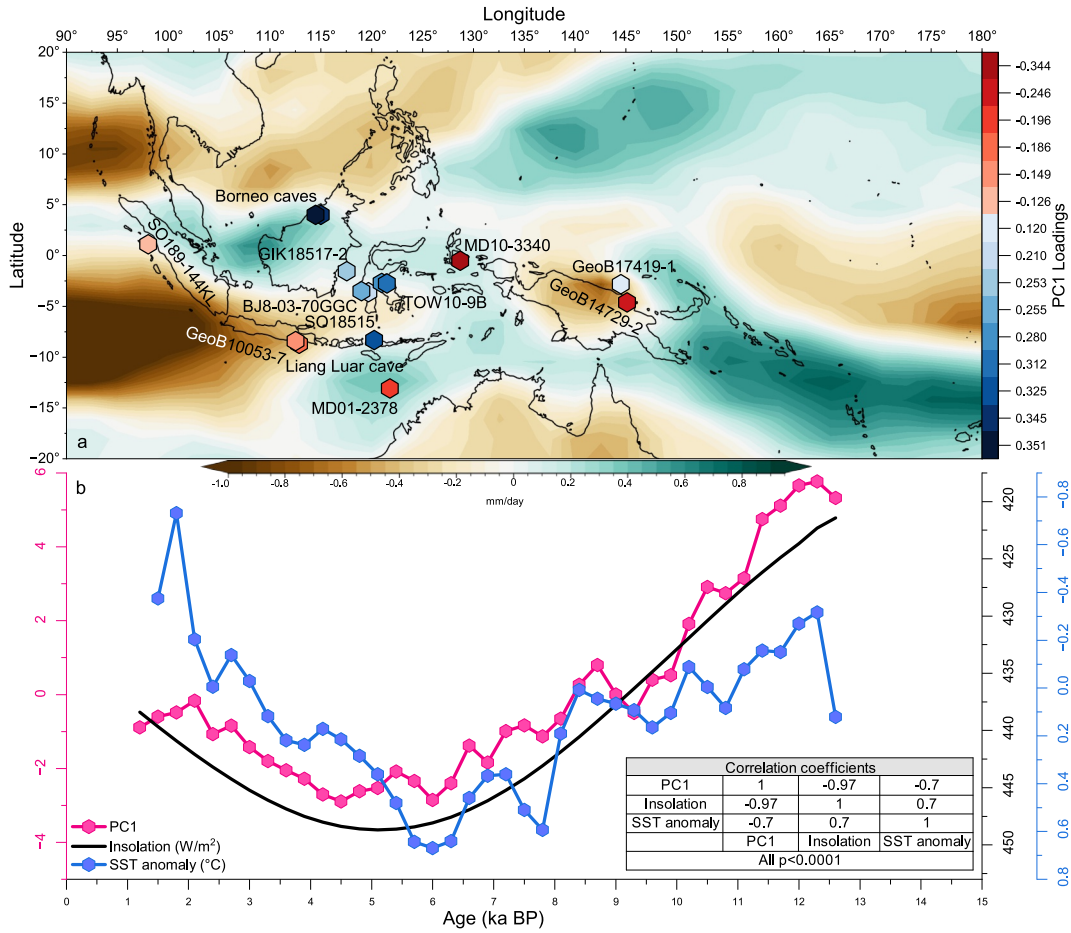


Figure 6. Principal component (PC1) Analysis (PCA) of precipitation-sensitive proxy records from the Maritime Continent (MC). (a) Spatial distribution of proxy sites with corresponding PC1 loadings and middle Holocene (7–4 ka BP) annual precipitation anomaly (shading, mm/day) derived from isotope-enabled Community Earth System Model 1.2 simulation; (b) PC1 scores (magenta) plotted against equatorial September insolation (black; Laskar et al., 2004), and zonal Pacific (western and eastern equatorial Pacific) sea surface temperature (SST) gradient anomaly (blue; Koutavas and Joanides, 2012a,b). PC1 explains ~45% of the total variance and shows a strong negative correlation with September insolation and positive relationship with the zonal Pacific SST gradient (see inlet table in panel b), suggesting that orbitally forced changes in the tropical Pacific mean state influenced rainfall distribution across the MC during the Holocene.

Additional evidence supporting La Niña-like condition comes from changes in the strength of the PWC, as intensified PWC is associated with La Niña conditions (McPhaden et al., 2006). Both MH proxy records and climate model simulations suggest a strengthened Walker Circulation during this period (Carré et al., 2014; Dang et al., 2020a; White et al., 2018). Collectively, these lines of evidence point to a strong likelihood of an ENSO-related, La Niña-like state that resulted in a decrease in rainfall over northern PNG during the MH. Our notion of a MH decrease in rainfall due to La Nina-like conditions is in good agreement with MH climate simulations, which show a SPCZ position that typically emerges under La Niña-like conditions (Brown et al., 2020; Mantsis et al., 2013). Although our iCEMS simulations were designed as orbital sensitivity experiments, rather than a transient Holocene experiment, the modeled isotopic response agrees with both reconstructed $\delta^2H_{precip\text{-}ic}$ values and modern GNIP observations (see Figure S4 and Table S1 in Supporting Information S1). Hence, we are confident that the model was able to capture the first-order hydroclimate control over our study area. Here, we examined annual and monthly $\delta^2H_{precipitation}$ and rainfall anomaly simulation from iCESM, which show substantially enriched $\delta^2H_{precipitation}$ values and reduced rainfall over PNG during the MH (Figures 4a, 4b, and 5). The simulation show that northern part of PNG experienced relatively dry conditions during the MH (7–4 ka BP-PI, Figure 4b). To understand how the annual rainfall anomaly translates into seasonal changes, we conducted a January to December iCESM precipitation simulation for the MH (Figure 6). We observed that during the MH

25724525, 2026, 10, Downloaded from https://agupubs.onlinelibrary.wiley.com/doi/10.1029/2026PA005515 by Xiamen University, Wiley Online Library on [28/10/2026]. See the Terms and Conditions (https://onlinelibrary.wiley.com/terms-and-conditions) on Wiley Online Library for rules of use; OA articles are governed by the applicable Creative Commons License

25724525, 2026, 10, Downloaded from https://agupubs.onlinelibrary.wiley.com/doi/10.1029/2026PA005515 by Xiamen University, Wiley Online Library on [28/10/2026]. See the Terms and Conditions (https://onlinelibrary.wiley.com/terms-and-conditions) on Wiley Online Library for rules of use; OA articles are governed by the applicable Creative Commons License

(~7–4 ka BP), northern PNG received less rainfall from November through August, followed by an increase in rainfall from September to October (Figure 5). This seasonal pattern is consistent with modern observations, which indicate that northern PNG experiences a significant decrease in rainfall during austral summer-to-autumn in La Niña years (Smith et al., 2013). Our model simulation results agree with climate model simulations by Zhang et al. (2022), that show reduced rainfall over PNG during the MH. In contrast, Dang et al. (2020a) report enhanced precipitation in the western equatorial Pacific under a strengthened Walker Circulation. This apparent discrepancy is likely attributed to differences in seasons analyzed. Dang et al. (2020a) primarily looked on October to December precipitation, while Zhang et al. (2022) focus on the January to June rainfall, illustrating that MH hydroclimate responses are strongly dependent on a seasonal scale. We suggest that although rainfall increases from August to October over northern PNG (Figure 5), it is insufficient to offset the pronounced reduction from November through July, resulting in an overall decrease in annual rainfall over PNG during the MH as shown in Figure 4b. Modern rainfall climatology shows that PNG receives most of its rainfall from October through May (see Figure 1). Thus, any suppression of rainfall during this interval would significantly reduce annual rainfall total amount. We therefore interpret the prolonged MH drying as evidence for a shift in the prevailing ENSO activity towards more La Niña-like conditions (Figures 4b and 5). Noteworthy, proxy indicators of continental (bulk marine sediment Fe/Ca, Ti/Ca, and K/Ca ratios) and marine rainfall and advection (sea surface salinity, SSS) from a sedimentary archive off the northern coast of PNG reveal a minimum in rainfall driven runoff and erosion during the MH (i.e., from 8 to 6 ka BP), followed by an abrupt transition, within ~1 ka, to wetter conditions during the Late Holocene (Bova et al., 2025). Bova et al. (2025) invoke a contraction of the tropical rain band and a MH strengthening of the PWC to explain rainfall variability in northern PNG during the Holocene. Although the timing of the MH drier conditions at both sites is slightly different, we suggest that both records support the concept that the decrease in rainfall over northern PNG is related to more persistent La Niña-like condition associated with a strengthened PWC, or alternatively a reduced El Niño frequency during the MH.

4.2. PCA Hydroclimate Mode

The coherent MH dry interval observed in our multiproxy record suggest that hydroclimate changes from northern PNG may reflect a broader reorganization of the MC rainfall. To investigate this possibility, we applied a compilation of precipitation-sensitive proxy records across the MC. PCA reveals a dominant hydroclimate mode (PC1) that accounts for ~45% of the data variance across rainfall-sensitive proxy records from the MC (Figures 6a and 6b). Spatial loadings indicate a tripole hydroclimate pattern, with negative PC1 values corresponding to reduced rainfall over NG and adjacent southwest MC sites, while positive PC1 values reflect wetter conditions over Borneo and Sulawesi. The PC1 time-series show a pronounced negative value during the MH (~7–4 ka BP), consistent with enriched δ^2H and $\delta^{13}C$ values and reduced ln (Ti/Ca) and ln (Fe/Ca) ratios recorded at GeoB17429-2 site. The agreement between PC1 and our multiproxy record indicates that MH dry interval as inferred from our site represent a regional reorganization of MC hydroclimate rather than an isolated, local signal. To investigate the drivers of this tripole hydroclimate mode, we examined the relationship between PC1 and equatorial September insolation. Near the equator, September experiences the highest seasonal insolation maxima, and changes in this peak have been linked to ENSO-related variability (Clement et al., 2000). Hence, mechanisms driving air-sea couplings (e.g., variations in the Walker and Hadley cell) are expected to follow September insolation changes (Clement et al., 1999). Indeed, PC1 shows a strong correlation with the equatorial September insolation ($r^2 = 0.97$, $p < 0.001$, Figure 6b), indicating that insolation-driven changes played a critical role in modulating this hydroclimate mode. Additional support is provided by the close agreement between the reconstructed $\delta^2H_{precip\text{-}ic}$ data and the zonal equatorial Pacific SST gradient (Koutavas and Joanides, 2012a, 2012b, Figure S8 in Supporting Information S1). The enriched $\delta^2H_{precip\text{-}ic}$ values between ~7–4 ka BP, interpreted as reduced rainfall over northern PNG, coincides with the strongest west-to-east equatorial Pacific SST gradient (see Figure 6b). Since the zonal SST gradient exerts a major control on the strength of the PWC (McPhaden et al., 2006), the close correspondence between the two records is consistent that the MH dry period over northern PNG was associated with a stronger PWC. This interpretation is further supported by the modeled atmospheric circulation response. During the MH (7–4 ka BP), the zonal mass steam function (ZMSF; Peixóto and Oort, 1984) shows chiefly positive anomalies across the tropical equatorial Pacific, indicating an intensification of the PWC (Figure S11 in Supporting Information S1). This anomaly is accompanied by coherent anomalies in vertical velocity and low-level zonal winds, consistent with enhanced zonal SST gradient and stronger PWC inferred from the proxy record. Hence, increased September insolation during the MH likely strengthened the trade winds, enhanced the zonal SST gradient across the equatorial Pacific (Figures 6b, Figure

25724525, 2026, 10, Downloaded from https://agupubs.onlinelibrary.wiley.com/doi/10.1029/2026PA005515 by Xiamen University, Wiley Online Library on [28/10/2026]. See the Terms and Conditions (https://onlinelibrary.wiley.com/terms-and-conditions) on Wiley Online Library for rules of use; OA articles are governed by the applicable Creative Commons License

S10 in Supporting Information S1). The higher SST gradient in turn, strengthened the PWC and redistributed rainfall across the MC. These changes likely altered the tropical Pacific mean state and associated atmospheric circulation, a mechanism that previously proposed by Chen et al. (2016a) and Dang et al. (2020a). In this configuration, Borneo and other northern sites experienced enhanced rainfall, whereas PNG and adjacent southwestern regions became drier, consistent with the tripole pattern revealed by PC1 loadings (Figure 6a). Our iCESM simulation reproduced reduced rainfall and isotopically enriched precipitation over northern PNG during the MH (Figure 4). The close agreement between PCA, SST gradient, iCESM simulation, and independent proxy records support a common mechanism in which orbitally-driven changes in the tropical Pacific mean state controlled the spatial distribution of rainfall across the MC during the MH.

5. Conclusions

Our multi-proxy hydroclimate reconstruction, supported by isotope-enabled climate simulations, reveals a pronounced and statistically significant reduction in rainfall over northern PNG during the MH (~7–4 ka BP). This dry period is consistently documented by enriched δ^2H and $\delta^{13}C$ values, indicative of reduced rainfall, together with diminished terrigenous runoff as inferred from XRF-derived ln (Fe/Ca) and ln (Ti/Ca) ratios. We suggest that the decrease in rainfall over PNG is related to more persistent La Niña-like condition associated with a strengthened PWC, or alternatively a reduced El Niño frequency during the MH time interval ~7–4 ka BP. A synthesis of precipitation-sensitive records across the MC using PCA identifies a dominant hydroclimate mode characterized by an antiphase rainfall pattern, with dry conditions over northern PNG and the southwestern MC, but wetter conditions over Borneo and Sulawesi. The strong coupling between this and equatorial September insolation demonstrates that orbital forcing modulated ENSO-like variability and the zonal mean state of the tropical Pacific, leading to regionally coherent, yet spatially contrasting responses. Collectively, our findings show that MH rainfall variability in the WPWP is not solely controlled by ITCZ migration. Instead, MH, insolation-driven changes in ENSO and Walker Circulation strength shifted the hydroclimate toward a more La Niña–like mean state. Hence, underscoring the importance of the role of ocean-atmosphere couplings when interpreting past hydroclimate variability. Our results highlight the sensitivity of PNG rainfall to changes in seasonal and interannual climate modes and provide a robust analogue for understanding, and anticipating, future hydroclimate responses in the WPWP under ongoing changes in the tropical Pacific mean state.

Conflict of Interest

The authors declare no conflicts of interest relevant to this study.

Availability Statement

The data sets of this study are archived at Zenodo (https://doi.org/10.5281/zenodo.19466813; Lázár et al., 2026). This includes the age model, plant-wax-derived *n*-alkanes and their stable carbon ($\delta^{13}C$) and hydrogen (δ^2H) isotopic compositions, and sediment elemental ratios (Fe/Ca and Ti/Ca) obtained by XRF core scanning from marine sediment core GeoB17429-2. The GPCP data (Adler et al., 2003) used in Figure 1a are available at https://www.nccs.nasa.gov/gpcp/. The monthly rainfall data from meteorological stations used in Figure 1a were provided by the National Weather Station of PNG (https://www.pngmet.gov.pg/). The equatorial September insolation (Laskar et al., 2004) shown in Figure 6b is available at https://ssp.imcce.fr/insola/earth/online/earth/earth.html (last accessed on 27th of September 2026). The zonal Pacific (western and eastern equatorial Pacific) SST gradient anomaly of Koutavas and Joanides (2012a) that are shown in Figure 6 can be found at the NOAA National Centers for Environmental Information (Koutavas and Joanides, 2012b). The precipitation-sensitive proxy records used for PC1 Analysis (PCA) presented in Table 2 and shown in Figure 6 can be accessed from PANGAEA (Dang et al., 2020b; Hendrizan et al., 2017; Hollstein et al., 2019; Mohtadi et al., 2011b; Niedermeyer et al., 2014b; Ruan et al., 2018; Zhang et al., 2020) and the NOAA National Centers for Environmental Information (Carolin et al., 2013b; Chen et al., 2016b; Griffiths et al., 2009b; Konecky et al., 2016; Parish et al., 2024b; Tierney et al., 2012b). The plant wax data reported by Wicaksono et al. (2017) were provided by the author upon request. OriginPro 2026 (version 10.3.0.180) was used for data analysis, figure preparation, and statistical analysis. *R* version 4.4.2 was used to perform the Monte Carlo Kolmogorov-Smirnov test to assess the significance of the relationship between $\delta^2H_{precip\text{-}ic}$ and age while accounting for analytical and age uncertainties.

Acknowledgments
We sincerely thank editor Sarah Feakins, Jim Russell, David Fastovich, and an anonymous reviewer for their thoughtful and careful evaluation of the manuscript and their constructive suggestion. Their input significantly improved the quality of this manuscript. This study was supported by a grant to SS and ZJ through the National Natural Science Foundation of China (NSFC No. 91958208), and the German Ministry of Education and Research to MM (BMBF No. 03G0228A). BL acknowledges financially support from the China Scholarship Council. We greatly appreciate the RV SONNE (Cruise SO-228) Captain, crew, and scientific party for their professional and constructive assistance. ES and MM acknowledge support from the Deutsche Forschungsgemeinschaft (DFG, German Research Foundation) under Germany's Excellence Strategy (EXC−2077-390741603). Ralph Kreutz is greatly appreciated for his guidance during the isotope analysis. We also thank the National Weather Service of PNG for providing the meteorological data.

References

Adler, R. F., Huffman, G. J., Chang, A., Ferraro, R., Xie, P.-P., Janowiak, J., et al. (2003). The Version-2 Global Precipitation Climatology Project (GPCP) monthly precipitation analysis (1979–Present). *Journal of Hydrometeorology*, *4*(6), 1147–1167. https://doi.org/10.1175/1525-7541(2003)004<1147:TVGPCP>2.0.CO;2

Aldrian, E., & Dwi Susanto, R. (2003). Identification of three dominant rainfall regions within Indonesia and their relationship to sea surface temperature. *International Journal of Climatology*, *23*(12), 1435–1452. https://doi.org/10.1002/joc.950

Bartlein, P. J., & Shafer, S. L. (2019). Paleo calendar-effect adjustments in time-slice and transient climate-model simulations (PaleoCalAdjust v1.0): Impact and strategies for data analysis. *Geoscientific Model Developemnt*, *12*(9), 3889–3913. https://doi.org/10.5194/gmd-12-3889-2019

Bintanja, R., Van De Wal, R. S. W., & Oerlemans, J. (2005). Modelled atmospheric temperatures and global sea levels over the past million years. *Nature*, *437*(7055), 125–128. https://doi.org/10.1038/nature03975

Blaauw, M., & Christen, J. A. (2011). Flexible paleoclimate age-depth models using an autoregressive gamma process. *Bayesian Analysis*, *6*(3), 457–474. https://doi.org/10.1214/11-BA618

Bourke, R. (2010). Altitudinal limits of 230 economic crop species in Papua New Guinea. In S. G. Harbel, J. Stevenson, & M. Prebble (Eds.), *Altered Ecologies: Fire, climate and human influence on terrestrial landscapes* (pp. 473–512). ANU ePress.

Bova, S. C., Rosenthal, Y., & Du, X. (2025). Contraction of the Western Pacific tropical rain Belt and weakening of the walker circulation: Future lessons from the past two interglacials. *Paleoceanography and Paleoclimatology*, *40*(4), e2024PA004997. https://doi.org/10.1029/2024PA004997

Brown, J. R., Lengaigne, M., Lintner, B. R., Widlansky, M. J., Van Der Wiel, K., Dutheil, C., et al. (2020). South Pacific Convergence Zone dynamics, variability and impacts in a changing climate. *Nature Reviews Earth and Environment*, *1*(10), 530–543. https://doi.org/10.1038/s43017-020-0078-2

Bush, R. T., & McInerney, F. A. (2013). Leaf wax n-alkane distributions in and across modern plants: Implications for paleoecology and chemotaxonomy. *Geochimica et Cosmochimica Acta*, *117*, 161–179. https://doi.org/10.1016/j.gca.2013.04.016

Carolin, S. A., Cobb, K. M., Adkins, J. F., Clark, B., Conroy, J. L., Lejau, S., et al. (2013a). Varied response of Western Pacific hydrology to climate forcings over the last glacial period. *Science*, *340*(6140), 1564–1566. https://doi.org/10.1126/science.1233797

Carolin, S. A., Cobb, K. M., Adkins, J. F., Clark, B., Conroy, J. L., Lejau, S., et al. (2013b). Borneo 100 - 15 KYrBP Stalagmite Oxygen Isotope Data. *NOAA National Centers for Environmental Information*. [Dataset]. https://doi.org/10.25921/axcs-h325

Carré, M., Sachs, J. P., Purca, S., Schauer, A. J., Braconnot, P., Falcón, R. A., et al. (2014). Holocene history of ENSO variance and asymmetry in the eastern tropical Pacific. *Science*, *345*(6200), 1045–1048. https://doi.org/10.1126/science.1252220

Carré, M., Sachs, J. P., Wallace, J. M., & Favier, C. (2012). Exploring errors in paleoclimate proxy reconstructions using Monte Carlo simulations: Paleotemperature from mollusk and coral geochemistry. *Climate of the Past*, *8*(2), 433–450. https://doi.org/10.5194/cp-8-433-2012

Chappell, J., & Polach, H. A. (1976). Holocene sea-level change and coral-reef growth at Huon Peninsula, Papua New Guinea. *Geological Society of America Bulletin*, *87*(2), 235–240. https://doi.org/10.1130/0016-7606(1976)87<235:HSCACG>2.0.CO;2

Chen, S., Hoffmann, S. S., Lund, D. C., Cobb, K. M., Emile-Geay, J., & Adkins, J. F. (2016a). A high-resolution speleothem record of western equatorial Pacific rainfall: Implications for Holocene ENSO evolution. *Earth and Planetary Science Letters*, *442*, 61–71. https://doi.org/10.1016/j.epsl.2016.02.050

Chen, S., Hoffmann, S. S., Lund, D. C., Cobb, K. M., Emile-Geay, J., & Adkins, J. F. (2016b). Borneo high resolution Holocene speleothem oxygen isotope data [Dataset]. *NOAA National Centers for Environmental Information*. https://doi.org/10.25921/c880-f473

Clement, A. C., Seager, R., & Cane, M. A. (1999). Orbital controls on the El Niño/Southern Oscillation and the tropical climate. *Paleoceanography*, *14*(4), 441–456. https://doi.org/10.1029/1999PA900013Digital

Clement, A. C., Seager, R., & Cane, M. A. (2000). Suppression of El Niño during the Mid-Holocene by changes in the Earth's orbit. *Paleoceanography*, *15*(6), 731–737. https://doi.org/10.1029/1999PA000466

Collins, J. A., Schefuß, E., Mulitza, S., Prange, M., Werner, M., Tharammal, T., et al. (2013). Estimating the hydrogen isotopic composition of past precipitation using leaf-waxes from western Africa. *Quaternary Science Reviews*, *65*, 88–101. https://doi.org/10.1016/j.quascirev.2013.01.007

Dang, H., Jian, Z., Kissel, C., & Bassinot, F. (2020b). Age and sediment geochemical data of MD10-3340, Halmahera Sea [Dataset]. *PANGAEA*. https://doi.org/10.1594/PANGAEA.924044

Dang, H., Jian, Z., Wang, Y., Mohtadi, M., Rosenthal, Y., Ye, L., et al. (2020a). Pacific warm pool subsurface heat sequestration modulated Walker circulation and ENSO activity during the Holocene. *Science Advances*, *6*(42), eabc0402. https://doi.org/10.1126/sciadv.abc0402

De Deckker, P. (2016). The Indo-Pacific Warm Pool: Critical to world oceanography and world climate. *Geoscience Letters*, *3*(1), 20. https://doi.org/10.1186/s40562-016-0054-3

Denniston, R. F., Wyrwoll, K.-H., Polyak, V. J., Brown, J. R., Asmerom, Y., Wanamaker, A. D., et al. (2013). A Stalagmite record of Holocene Indonesian–Australian summer monsoon variability from the Australian tropics. *Quaternary Science Reviews*, *78*, 155–168. https://doi.org/10.1016/j.quascirev.2013.08.004

Diefendorf, A. F., & Freimuth, E. J. (2017). Extracting the most from terrestrial plant-derived n-alkyl lipids and their carbon isotopes from the sedimentary record: A review. *Organic Geochemistry*, *103*, 1–21. https://doi.org/10.1016/j.orggeochem.2016.10.016

Donohoe, A., Marshall, J., Ferreira, D., & McGee, D. (2013). The relationship between ITCZ location and cross-equatorial atmospheric heat transport: From the seasonal cycle to the last glacial maximum. *Journal of Climate*, *26*(11), 3597–3618. https://doi.org/10.1175/jcli-d-12-00467.1

Dubois, N., Oppo, D. W., Galy, V. V., Mohtadi, M., van der Kaars, S., Tierney, J. E., et al. (2014). Indonesian vegetation response to changes in rainfall seasonality over the past 25,000 years. *Nature Geoscience*, *7*(7), 513–517. https://doi.org/10.1038/ngeo2182

Eglinton, G., & Hamilton, R. J. (1967). Leaf epicuticular waxes. *Science*, *156*(3780), 1322–1335. https://doi.org/10.1126/science.156.3780.1322

Falster, G., Konecky, B., Madhavan, M., Stevenson, S., & Coats, S. (2021). Imprint of the Pacific walker circulation in global precipitation δ18O. *Journal of Climate*, *34*(21), 8579–8597. https://doi.org/10.1175/JCLI-D-21-0190.1

Farquhar, G. D., Ehleringer, J. R., & Hubick, K. T. (1989). Carbon isotope discrimination and photosynthesis. *Annual Review of Plant Biology*, *40*(1), 503–537. https://doi.org/10.1146/annurev.pp.40.060189.002443

Feakins, S. J., & Sessions, A. L. (2010). Controls on the D/H ratios of plant leaf waxes in an arid ecosystem. *Geochimica et Cosmochimica Acta*, *74*(7), 2128–2141. https://doi.org/10.1016/j.gca.2010.01.016

Gao, L., Edwards, E. J., Zeng, Y., & Huang, Y. (2014). Major evolutionary trends in hydrogen isotope fractionation of vascular plant leaf waxes. *PLoS One*, *9*(11), e112610. https://doi.org/10.1371/journal.pone.0112610

25724525, 2026, 10, Downloaded from https://agupubs.onlinelibrary.wiley.com/doi/10.1029/2026PA005515 by Xiamen University, Wiley Online Library on [28/10/2026]. See the Terms and Conditions (https://onlinelibrary.wiley.com/terms-and-conditions) on Wiley Online Library for rules of use; OA articles are governed by the applicable Creative Commons License

Garcin, Y., Schefuß, E., Schwab, V. F., Garreta, V., Gleixner, G., Vincens, A., et al. (2014). Reconstructing C3 and C4 vegetation cover using n-alkane carbon isotope ratios in recent lake sediments from Cameroon, Western Central Africa. *Geochimica et Cosmochimica Acta*, *142*, 482–500. https://doi.org/10.1016/j.gca.2014.07.004

Griffiths, M. L., Drysdale, R. N., Gagan, M. K., Zhao, J. X., Ayliffe, L. K., Hellstrom, J. C., et al. (2009a). Increasing Australian–Indonesian monsoon rainfall linked to early Holocene sea-level rise. *Nature Geoscience*, *2*(9), 636–639. https://doi.org/10.1038/ngeo605

Griffiths, M. L., Drysdale, R. N., Gagan, M. K., Zhao, J.-X., Ayliffe, L. K., Hellstrom, J. C., et al. (2009b). Griffiths et al. 2009 Liang Luar Indonesia Stalagmite d18O Data [Dataset]. *NOAA National Centers for Environmental Information*. https://doi.org/10.25921/m36w-f623

Heaton, T. J., Köhler, P., Butzin, M., Bard, E., Reimer, R. W., Austin, W. E. N., et al. (2020). Marine20—The marine radiocarbon Age calibration curve (0–55,000 cal BP). *Radiocarbon*, *62*(4), 779–820. https://doi.org/10.1017/RDC.2020.68

Hendrizan, M., Kuhnt, W., & Holbourn, A. E. (2017). Seawater $\delta^{18}O$ reconstruction for sediment core GIK18517-2 [Dataset]. *PANGAEA*. https://doi.org/10.1594/PANGAEA.880965

Hoetzel, S., Dupont, L., Schefuß, E., Rommerskirchen, F., & Wefer, G. (2013). The role of fire in Miocene to Pliocene C4 grassland and ecosystem evolution. *Nature Geoscience*, *6*(12), 1027–1030. https://doi.org/10.1038/ngeo1984

Hollstein, M., Mohtadi, M., Rosenthal, Y., Prange, M., Oppo, D. W., Martínez-Méndez, G., et al. (2019). Planktic foraminiferal Mg/Ca, Nd/Ca and oxygen isotopes and XRF core scanner data (Ti/Ca) of sediment core GeoB17419-1 [Dataset]. *PANGAEA*. https://doi.org/10.1594/PANGAEA.899182

Hope, G. (2014). The sensitivity of the high Mountain ecosystems of new Guinea to climatic change and anthropogenic impact. *Arctic Antarctic and Alpine Research*, *46*(4), 777–786. https://doi.org/10.1657/1938-4246-46.4.777

Jackson, D. A. (1993). Stopping rules in principal components analysis: A comparison of heuristical and statistical approaches. *Ecology*, *74*(8), 2204–2214. https://doi.org/10.2307/1939574

Jia, X., Ge, J., & Wang, S. (2016). Diverse impacts of ENSO on wintertime rainfall over the Maritime Continent. *International Journal of Climatology*, *36*(9), 3384–3397. https://doi.org/10.1002/joc.4562

Kahmen, A., Hoffmann, B., Schefuß, E., Arndt, S. K., Cernusak, L. A., West, J. B., & Sachse, D. (2013b). Leaf water deuterium enrichment shapes leaf wax n-alkane δD values of angiosperm plants II: Observational evidence and global implications. *Geochimica et Cosmochimica Acta*, *111*, 50–63. https://doi.org/10.1016/j.gca.2012.09.004

Kahmen, A., Schefuß, E., & Sachse, D. (2013a). Leaf water deuterium enrichment shapes leaf wax n-alkane δD values of angiosperm plants I: Experimental evidence and mechanistic insights. *Geochimica et Cosmochimica Acta*, *111*, 39–49. https://doi.org/10.1016/j.gca.2012.09.003

Konecky, B. L., Noone, D. C., & Cobb, K. M. (2019). The influence of competing hydroclimate processes on stable isotope ratios in tropical rainfall. *Geophysical Research Letters*, *46*(3), 1622–1633. https://doi.org/10.1029/2018GL080188

Konecky, B. L., Russell, J. M., & Bijaksana, S. (2016). Lake towuti, Indonesia 60,000 year leaf wax hydrogen isotope data [Dataset]. *NOAA National Centers for Environmental Information*. https://doi.org/10.25921/qqd9-q059

Koutavas, A., & Joanides, S. (2012a). El niño-southern oscillation extrema in the Holocene and last glacial maximum. *Paleoceanography*, *27*(4), PA4208. https://doi.org/10.1029/2012pa002378

Koutavas, A., & Joanides, S. (2012b). Eastern equatorial Pacific LGM-Holocene G. ruber d18O data [Dataset]. *NOAA National Centers for Environmental Information*. https://doi.org/10.25921/qznc-m246

Kuhnt, W., Holbourn, A., Xu, J., Opdyke, B., De Deckker, P., Röhl, U., & Mudelsee, M. (2015). Southern Hemisphere control on Australian monsoon variability during the late deglaciation and Holocene. *Nature Communications*, *6*(1), 5916. https://doi.org/10.1038/ncomms6916

Laskar, J., Robutel, P., Joutel, F., Gastineau, M., Correia, A. C. M., & Levrard, B. (2004). A long-term numerical solution for the insolation quantities of the Earth. *Astronomy and Astrophysics*, *428*(1), 261–285. https://doi.org/10.1051/0004-6361:20041335

Lázár, B., Mohtadi, M., Yang, Y.-C., Hu, J., Schefuß, E., Jian, Z., et al. (2026). Hydroclimate Variability in the Western Pacific Warm Pool over the last 15 kyr [Dataset]. *Zenodo*. https://doi.org/10.5281/zenodo.19466813

Lentfer, C., Pavlides, C., & Specht, J. (2010). Natural and human impacts in a 35 000-year vegetation history in central New Britain, Papua New Guinea. *Quaternary Science Reviews*, *29*(27), 3750–3767. https://doi.org/10.1016/j.quascirev.2010.08.009

Lintner, B. R., & Boos, W. R. (2019). Using atmospheric energy transport to quantitatively constrain south Pacific convergence Zone shifts during ENSO. *Journal of Climate*, *32*(6), 1839–1855. https://doi.org/10.1175/jcli-d-18-0151.1

Locarnini, R. A., Mishonov, A. V., Antonov, J. I., Boyer, T. P., Garcia, H. E., Baranova, O. K., et al. (2013). *World Ocean Atlas 2013* (Vol. 1). Temperature. https://doi.org/10.7289/V55X26VD

Mantsis, D. F., Lintner, B. R., Broccoli, A. J., & Khodri, M. (2013). Mechanisms of mid-holocene precipitation change in the South Pacific convergence Zone. *Journal of Climate*, *26*(18), 6937–6953. https://doi.org/10.1175/jcli-d-12-00674.1

Marchitto, T. M., Muscheler, R., Ortiz, J. D., Carriquiry, J. D., & van Geen, A. (2010). Dynamical response of the tropical Pacific Ocean to solar forcing during the early Holocene. *Science*, *330*(6009), 1378–1381. https://doi.org/10.1126/science.1194887

McClelland, H. L. O., Halevy, I., Wolf-Gladrow, D. A., Evans, D., & Bradley, A. S. (2021). Statistical uncertainty in paleoclimate proxy reconstructions. *Geophysical Research Letters*, *48*(15), e2021GL092773. https://doi.org/10.1029/2021GL092773

McGregor, H. V., Gagan, M. K., McCulloch, M. T., Hodge, E., & Mortimer, G. (2008). Mid-Holocene variability in the marine 14C reservoir age for northern coastal Papua New Guinea. *Quaternary Geochronology*, *3*(3), 213–225. https://doi.org/10.1016/j.quageo.2007.11.002

McKay, N. P., Emile-Geay, J., & Khider, D. (2021). geoChronR – An R package to model, analyze, and visualize age-uncertain data. *Geochronology*, *3*(1), 149–169. https://doi.org/10.5194/gchron-3-149-2021

McPhaden, M. J., Zebiak, S. E., & Glantz, M. H. (2006). ENSO as an integrating concept in Earth science. *Science*, *314*(5806), 1740–1745. https://doi.org/10.1126/science.1132588

Mohtadi, M., Bergmann, F., Blanquera, R. V. C., Buleka, J., Carag, J. W. M., Carriérre-Garwood, J., et al. (2013). *Report and preliminary results of RV SONNE cruise SO-228, Kaohsiung-Townsville, 04.05. 2013-23.06. 2013, EISPAC-WESTWIND-SIODP*. Berichte, MARUM Zentrum für Marine Umweltwissenschaften, Fachbereich-Geowissenschaften, Universität Bremen, No. 295, 110 pages, Bremen.

Mohtadi, M., Oppo, D. W., Steinke, S., Stuut, J.-B. W., De Pol-Holz, R., Hebbeln, D., & Lückge, A. (2011a). Glacial to Holocene swings of the Australian–Indonesian monsoon. *Nature Geoscience*, *4*(8), 540–544. https://doi.org/10.1038/ngeo1209

Mohtadi, M., Oppo, D. W., Steinke, S., Stuut, J.-B. W., De Pol-Holz, R., Hebbeln, D., & Lückge, A. (2011b). Logarithmic ratio between titanium and calcium [Dataset]. *PANGAEA*. https://doi.org/10.1594/PANGAEA.767352

Neale, R., & Slingo, J. (2003). The Maritime continent and its role in the global climate: A GCM Study. *Journal of Climate*, *16*(5), 834–848. https://doi.org/10.1175/1520-0442(2003)016<0834:tmcair>2.0.co;2

Niedermeyer, E. M., Sessions, A. L., Feakins, S. J., & Mohtadi, M. (2014a). Hydroclimate of the western Indo-Pacific Warm Pool during the past 24,000 years. *Proceedings of the National Academy of Sciences*, *111*(26), 9402–9406. https://doi.org/10.1073/pnas.1323585111

Niedermeyer, E. M., Sessions, A. L., Feakins, S. J., & Mohtadi, M. (2014b). Stable carbon and hydrogen isotope record of n-Alkanoic acids of sediment core SO189/2_144KL [Dataset]. *PANGAEA*. https://doi.org/10.1594/PANGAEA.836163

25724525, 2026, 10, Downloaded from https://agupubs.onlinelibrary.wiley.com/doi/10.1029/2026PA005515 by Xiamen University, Wiley Online Library on [28/10/2026]. See the Terms and Conditions (https://onlinelibrary.wiley.com/terms-and-conditions) on Wiley Online Library for rules of use; OA articles are governed by the applicable Creative Commons License

Nott, J., & Price, D. (1994). Plunge pools and paleoprecipitation. *Geology*, *22*(11), 1047–1050. https://doi.org/10.1130/0091-7613(1994)022<1047:PPAP>2.3.CO;2

Paijmans, K. (1976). *New Guinea vegetation*. Australian National University. Retrieved from http://hdl.handle.net/1885/114816

Parish, M., Russell, J., Konecky, B., Du, X., He, C., Bijaksana, S., & Vogel, H. (2024a). Changes in Indo-Pacific Warm Pool hydroclimate and vegetation during the last deglaciation. *Quaternary Science Reviews*, *336*, 108755. https://doi.org/10.1016/j.quascirev.2024.108755

Parish, M. C., Russell, J. M., Konecky, B. L., Du, X., He, C., Bijaksana, S., & Vogel, H. (2024b). Towuti and Matano Lake (Indonesia) n-alkane data over the past 30 kiloyears [Dataset]. *NOAA National Centers for Environmental Information*. https://doi.org/10.25921/gjsk-jn37

Peixóto, J. P., & Oort, A. H. (1984). Physics of climate. *Reviews of Modern Physics*, *56*(3), 365–429. https://doi.org/10.1103/RevModPhys.56.365

Petchey, F., & Ulm, S. (2012). Marine Reservoir variation in the Bismarck Region: An evaluation of spatial and temporal change in ΔR and R over the last 3000 years. *Radiocarbon*, *54*(1), 45–58. https://doi.org/10.2458/azu_js_rc.v54i1.13050

Petchey, F., Ulm, S., David, B., McNiven, I. J., Asmussen, B., Tomkins, H., et al. (2013). High-resolution radiocarbon dating of marine materials in archaeological contexts: Radiocarbon marine reservoir variability between Anadara, Gafrarium, Batissa, Polymesoda spp. and Echinoidea at Caution Bay, Southern Coastal Papua New Guinea. *Archaeological and Anthropological Sciences*, *5*(1), 69–80. https://doi.org/10.1007/s12520-012-0108-1

Qian, J.-H., Robertson, A. W., & Moron, V. (2010). Interactions among ENSO, the monsoon, and diurnal cycle in rainfall variability over Java, Indonesia. *Journal of the Atmospheric Sciences*, *67*(11), 3509–3524. https://doi.org/10.1175/2010jas3348.1

Qian, J.-H., Robertson, A. W., & Moron, V. (2013). Diurnal cycle in different weather regimes and rainfall variability over borneo associated with ENSO. *Journal of Climate*, *26*(5), 1772–1790. https://doi.org/10.1175/jcli-d-12-00178.1

Rauniyar, S. P., & Walsh, K. J. E. (2013). Influence of ENSO on the diurnal cycle of rainfall over the maritime continent and Australia. *Journal of Climate*, *26*(4), 1304–1321. https://doi.org/10.1175/jcli-d-12-00124.1

Rommerskirchen, F., Plader, A., Eglinton, G., Chikaraishi, Y., & Rullkötter, J. (2006). Chemotaxonomic significance of distribution and stable carbon isotopic composition of long-chain alkanes and alkan-1-ols in C4 grass waxes. *Organic Geochemistry*, *37*(10), 1303–1332. https://doi.org/10.1016/j.orggeochem.2005.12.013

Rozanski, K., Araguás-Araguás, L., & Gonfiantini, R. (1993). Isotopic patterns in modern global precipitation. In P. K. Swart, K. C. Lohmann, J. Mckenzie, & S. Savin (Eds.), *Climate change in Continental isotopic records* (Vol. 78, pp. 1–36). Geophysical Monograph Series. https://doi.org/10.1029/GM078p0001

Ruan, Y., Mohtadi, M., van der Kaars, S., Dupont, L. M., Hebbeln, D., & Schefuß, E. (2018). N-alkane homologue records (stable hydrogen and carbon isotopes, concentrations) of sediment core GeoB10053-7 [Dataset]. *PANGAEA*. https://doi.org/10.1594/PANGAEA.895892

Ruan, Y., Mohtadi, M., van der Kaars, S., Dupont, L. M., Hebbeln, D., & Schefuß, E. (2019). Differential hydro-climatic evolution of East Javanese ecosystems over the past 22,000 years. *Quaternary Science Reviews*, *218*, 49–60. https://doi.org/10.1016/j.quascirev.2019.06.015

Russell, J. M., Vogel, H., Konecky, B. L., Bijaksana, S., Huang, Y., Melles, M., et al. (2014). Glacial forcing of central Indonesian hydroclimate since 60,000 y B.P. *Proceedings of the National Academy of Sciences*, *111*(14), 5100–5105. https://doi.org/10.1073/pnas.1402373111

Sachse, D., Billault, I., Bowen, G. J., Chikaraishi, Y., Dawson, T. E., Feakins, S. J., et al. (2012). Molecular paleohydrology: Interpreting the hydrogen-isotopic composition of lipid biomarkers from photosynthesizing organisms. *Annual Review of Earth and Planetary Sciences*, *40*(1), 221–249. https://doi.org/10.1146/annurev-earth-042711-105535

Schefuß, E., Ratmeyer, V., Stuut, J.-B. W., Jansen, J. H. F., & Sinninghe Damsté, J. S. (2003). Carbon isotope analyses of n-alkanes in dust from the lower atmosphere over the central eastern Atlantic. *Geochimica et Cosmochimica Acta*, *67*(10), 1757–1767. https://doi.org/10.1016/S0016-7037(02)01414-X

Schneider, T., Bischoff, T., & Haug, G. H. (2014). Migrations and dynamics of the intertropical convergence zone. *Nature*, *513*(7516), 45–53. https://doi.org/10.1038/nature13636

Shi, G., Yan, H., Zhang, W., Liu, Z., Zhao, N., Dodson, J., et al. (2025). Modulation of inter-hemispheric temperature gradients on the Holocene Asian-Australian summer monsoon. *Nature Communications*, *17*(1), 1183. https://doi.org/10.1038/s41467-025-67951-7

Shi, X., Werner, M., Krug, C., Brierley, C. M., Zhao, A., Igbinosa, E., et al. (2022). Calendar effects on surface air temperature and precipitation based on model-ensemble equilibrium and transient simulations from PMIP4 and PACMEDY. *Climate of the Past*, *18*(5), 1047–1070. https://doi.org/10.5194/cp-18-1047-2022

Smith, I., Moise, A., Inape, K., Murphy, B., Colman, R., Power, S., & Chung, C. (2013). ENSO-related rainfall changes over the New Guinea region. *Journal of Geophysical Research: Atmospheres*, *118*(19), 10665–10675. https://doi.org/10.1002/jgrd.50818

Srivastava, K., & Wiesenberg, G. L. B. (2018). Severe drought-influenced composition and δ13C of plant and soil n-alkanes in model temperate grassland and heathland ecosystems. *Organic Geochemistry*, *116*, 77–89. https://doi.org/10.1016/j.orggeochem.2017.11.002

Steinke, S., Mohtadi, M., Prange, M., Varma, V., Pittauerova, D., & Fischer, H. W. (2014). Mid-to Late-Holocene Australian–Indonesian summer monsoon variability. *Quaternary Science Reviews*, *93*, 142–154. https://doi.org/10.1016/j.quascirev.2014.04.006

Tierney, J. E., Oppo, D. W., Legrande, A. N., Huang, Y., Rosenthal, Y., & Linsley, B. K. (2012a). The influence of Indian Ocean atmospheric circulation on Warm Pool hydroclimate during the Holocene epoch. *Journal of Geophysical Research*, *117*(D19), D19108. https://doi.org/10.1029/2012jd018060

Tierney, J. E., Oppo, D. W., LeGrande, A. N., Huang, Y., Rosenthal, Y., & Linsley, B. K. (2012b). Makassar Strait 14,700 year leaf wax hydrogen isotope data [Dataset]. *NOAA National Centers for Environmental Information*. https://doi.org/10.25921/s8sh-1059

Tuckman, P. J., Smyth, J., Lutsko, N. J., & Marshall, J. (2024). The zonal seasonal cycle of tropical precipitation: Introducing the indo-pacific monsoonal mode. *Journal of Climate*, *37*(14), 3807–3824. https://doi.org/10.1175/jcli-d-23-0125.1

Ulm, S., O'Grady, D., Petchey, F., Hua, Q., Jacobsen, G., Linnenlucke, L., et al. (2023). Australian marine radiocarbon reservoir effects: ΔR atlas and ΔR calculator for Australian mainland coasts and near-shore islands. *Radiocarbon*, *65*(5), 1139–1159. https://doi.org/10.1017/RDC.2023.95

Wang, H., & Mehta, V. M. (2008). Decadal variability of the indo-pacific warm pool and its Association with atmospheric and Oceanic variability in the NCEP–NCAR and SODA reanalyses. *Journal of Climate*, *21*(21), 5545–5565. https://doi.org/10.1175/2008jcli2049.1

Wang, Y., & Sessions, A. L. (2008). Memory effects in compound-specific D/H analysis by gas Chromatography/Pyrolysis/Isotope-Ratio mass spectrometry. *Analytical Chemistry*, *80*(23), 9162–9170. https://doi.org/10.1021/ac801170v

White, S. M., Ravelo, A. C., & Polissar, P. J. (2018). Dampened El niño in the early and mid-holocene due to insolation-forced Warming/Deepening of the thermocline. *Geophysical Research Letters*, *45*(1), 316–326. https://doi.org/10.1002/2017gl075433

Whitfeld, T. J. S., Lasky, J. R., Damas, K., Sosanika, G., Molem, K., & Montgomery, R. A. (2014). Species richness, Forest structure, and functional diversity during succession in the new Guinea lowlands. *Biotropica*, *46*(5), 538–548. https://doi.org/10.1111/btp.12136

Wicaksono, S. A., Russell, J. M., Holbourn, A., & Kuhnt, W. (2017). Hydrological and vegetation shifts in the Wallacean region of central Indonesia since the last Glacial Maximum. *Quaternary Science Reviews*, *157*, 152–163. https://doi.org/10.1016/j.quascirev.2016.12.006

25724525, 2026, 10, Downloaded from https://agupubs.onlinelibrary.wiley.com/doi/10.1029/2026PA005515 by Xiamen University, Wiley Online Library on [28/10/2026]. See the Terms and Conditions (https://onlinelibrary.wiley.com/terms-and-conditions) on Wiley Online Library for rules of use; OA articles are governed by the applicable Creative Commons License

Zhang, P., Xu, J., Holbourn, A. E., Kuhnt, W., Beil, S., Li, T., et al. (2020). Measurements of sediments from Core MD01-2378 and IODP Site 363-U1483 [Dataset]. *PANGAEA*. https://doi.org/10.1594/PANGAEA.918054

Zhang, X., Atwood, A. R., Nag, B., & Cobb, K. M. (2022). The tropical Pacific annual cycle and ENSO in PMIP4 simulations of the Mid-Holocene. *Journal of Geophysical Research: Oceans*, *127*(8), e2021JC017587. https://doi.org/10.1029/2021JC017587

References From the Supporting Information

Bray, E. E., & Evans, E. D. (1961). Distribution of n-paraffins as a clue to recognition of source beds. *Geochimica et Cosmochimica Acta*, *22*(1), 2–15. https://doi.org/10.1016/0016-7037(61)90069-2

Carr, A. S., Boom, A., Grimes, H. L., Chase, B. M., Meadows, M. E., & Harris, A. (2014). Leaf wax n-alkane distributions in arid zone South African flora: Environmental controls, chemotaxonomy and palaeoecological implications. *Organic Geochemistry*, *67*, 72–84. https://doi.org/10.1016/j.orggeochem.2013.12.004

Dang, H., Jian, Z., Kissel, C., & Bassinot, F. (2015). Precessional changes in the western equatorial Pacific Hydroclimate: A 240 kyr marine record from the Halmahera Sea, East Indonesia. *Geochemistry, Geophysics, Geosystems*, *16*(1), 148–164. https://doi.org/10.1002/2014GC005550

Häggi, C., Sawakuchi, A. O., Chiessi, C. M., Mulitza, S., Mollenhauer, G., Sawakuchi, H. O., et al. (2016). Origin, transport and deposition of leaf-wax biomarkers in the Amazon Basin and the adjacent Atlantic. *Geochimica et Cosmochimica Acta*, *192*, 149–165. https://doi.org/10.1016/j.gca.2016.07.002

25724525, 2026, 10, Downloaded from https://agupubs.onlinelibrary.wiley.com/doi/10.1029/2026PA005515 by Xiamen University, Wiley Online Library on [28/10/2026]. See the Terms and Conditions (https://onlinelibrary.wiley.com/terms-and-conditions) on Wiley Online Library for rules of use; OA articles are governed by the applicable Creative Commons License